RUN-UP OF SOLITARY WAVES

BY

Erika Kristina Lindstrøm

THESIS

for the degree of

MASTER OF SCIENCE

(Master i Anvendt matematikk og mekanikk)

Faculty of Mathematics and Natural Sciences
University of Oslo

June 2011

Det matematisk- naturvitenskapelige fakultet
Universitetet i Oslo

RUN-UP OF SOLITARY WAVES

by

Erika Kristina Lindstrøm

Abstract

This thesis presents experiments on run-up of solitary waves on a beach of 10° inclination. The purpose of this study is to find out what causes the lower maximum run-up heigths in experimental results compared with results from numerical models that are based on dispersive long wave theory and full potential theory. The experimental work includes the surface elevation, the velocity field close to the beach and tracing of the moving shoreline. It is found that the main devitation from theory appears in the later stage of the inundation. And the conclusion made is that the descripencies between theory and experiment are most likely due to viscous effects in the boundary layer.

Acknowledgments

First of all I would like to thank my supervisors professor Atle Jensen and professor Geir Pedersen for their support and guidance. Whenever I had questions, needed guidence in the laboratory or help with the simulations they always took their time to help me. I would also like to thank laboratory engineer Svein Vesterby for his assistance in the laboratory and for encouraging me when things where looking dark. I would like to thank PhD student Jostein Kolaas for the introduction of PIV technique and for helping me out whenever matlab refused to cooperate with me. MSc Trine Jelstad Olsen took her time to help me out with the mystery of English grammar, and I am very grateful for that.
Finally, I would like to thank my family. My two children Maja and Noah who always got me into a good mood and kept me going the times I felt like giving up. My dear husband Joakim Berglund who has been supporting and encouraging me during my studies, and taking care of our two children when I had to work evenings and weekends. Whitout him I would not have come this far.

Contents

Chapter 1

Introduction

1.1 Previous work and motivation

The run-up of waves on beaches is an important topic for the understanding and prediction of coastal impact of tsunamis. Tsunamis are sea waves most often generated by earthquakes or landslides, and they are considered long waves with small amplitude. Tsunamis travel with high speed over long distances. As they reach the coast, the amplitude of the wave is gaining and the wave travels inland potentially causing large property damage and loss of life. For example, the tsunami in Japan in mars 2011 caused thousands of deaths and widespread destruction.

Solitary waves have often been used in experiments concerning tsunami investigations. The advantage of studying solitary waves is that they are easy to generate in a wave tank. Also the waves are easy to reproduce as they are described by a single parameter, for example the amplitude. A shortcoming in using solitary waves when investigating tsunamis, is that they are, unlike tsunamis, both nonlinear and dispersive. Regardless, the investigation of the run-up of solitary waves plays an important role in the validation of numerical simulations and the understanding of the physics of the run-up.

The run-up of solitary waves have been investigated for decades and is an important topic. The theory applied has traditionally been long wave theory and the viscosity has been neglected. Pedersen & Gjevik [1] have presented a numerical model based on the Boussinesq equations for the simulation of run-up of non-breaking solitary waves. They compared the model with experimental data on a relatively steep beach (inclination of $\geq 20°$) and found good agreement with experimental results for inclinations of $> 20°$. For an inclination of $20°$ the numerical model overpredicted the maximum run-up height compared to the experimental results. Pedersen & Gjevik also found that the agreement

between numerical results and theoretical results where dependent of the equilibrium depth, observing the best agreement for deeper water. They suggested that these effects where caused by surface tension and frictional effects. Synolakis [2] studied run-up of breaking and non-breaking solitary waves on plane beaches with focus on maximum run-up heights and wave breaking. He derived an analytical run-up law based on an approximate solution of the nonlinear shallow water theory for prediction of maximum run-up height of solitary waves, and validated the formula with experimental results for different beach inclinations and wave amplitudes and found that the agreement was satisfactory. Synolakis also found that the increase in R/d with A/d, where R is the run-up height d is the equilibrium depth and A is the amplitude of the incident wave, is smaller for breaking waves than for non-breaking waves. Li & Raichlen (2001) [3] studied run-up of non-breaking waves on a beach with inclination of 25.7°. They derived a nonlinear solution to the shallow water equation, including higher order terms than the solution derived by Synolakis [2]. The results revealed that the agreement was good, but that the theory overestimated the tip of the run-up tongue. Li & Raichlen (2002) [4] investigated non-breaking and breaking solitary wave run-up on a beach with inclination of 3.8°. Most of the waves were breaking, but the results revealed a tendency of overprediction in maximum run-up height according to the numerical results. The data also revealed an increasing R/d with increasing depth when A/d was kept constant. Jensen *et al* [5] investigated run-up of solitary waves on a beach of 10.54° inclination and compared the maximum run-up height with a Boussinesq model and the run-up law from Synolakis [2]. They found that for the smallest incident wave the experimental results agreed well with the theory, but that the long-wave theories overestimated the run-up heights for the higher waves. Sælevik [6] investigated run-up of solitary waves on a straight beach with inclination of 10° and composite beach with change in the 10° inclination to 4° at a vertex point above the equilibrium water level. He compared the measured run-up heights for the straight beach with the Boussinesq equations and found that the results from the Boussinesq equations gave consistently lower run-up values compared with the experimental results. Sælevik also did PIV measurements in the flow during run-up and the results revealed the appearance of a boundary layer in the region close to the beach.

The articles mentioned above investigate various aspects of the run-up process, but they all have shown that the maximum run-up height in the experimental results is smaller compared to the numerical and analytical prediction. Suggestions are made that the viscous effects causes this deviation. So far no work has been done on trying to include the viscous effects in the numerical models.

Even though the boundary layer underneath a solitary wave during run-up has not been documented in the literature, investigations of the boundary layer underneath a solitary wave propagating on constant depth has been performed. Liu

et al [7] investigated the boundary layer under a solitary wave propagating at constant depth in a wavetank and found that the boundary layers was laminar and flow reversal started in the boundary layer as the flow at the outer edge of the boundary layer began to decelerate. No separation was observed and the agreement between numerical and experimental results were excellent. Sumer *et al* [8] investigated solitary wave boundary layers, simulated by solitary motion in an oscillating water tunnel. They found that transition to turbulence occurs at a Reynolds number $Re_{cr} = 5 \times 10^5$. The boundary layer is laminar for $Re < 2 \times 10^5$, and at the range $2 \times 10^5 < Re < 5 \times 10^5$ a regular array of vortices emerges near the bed. Liu *et al* also found that the flow reversal is delayed quite substantially with increasing Reynolds number

This thesis further investigates the run-up of a solitary wave on a sloped beach. The main target is to find out what causes the overprediction of the maximum run-up height in the theoretical results compared with experimental results. In this study the beach has an inclination of 10° and there are five different incoming waves generated. The five waves have different amplitude to depth ratio A/d = [0.0977, 0.195, 0.292, 0.388, 0.481] where A is the amplitude and the equilibrium depth d is kept constant at 20.0 cm.

1.2 Contents of the thesis

In Chapter 2 a brief introduction of the theory applied in the numerical models are presented. The three main theories are potential theory, dispersive nonlinear long wave theory and boundary layer theory. A short description of Lagrangian and Eularian representation of particle motion in a fluid is also given, as well as the different wave regimes and the governing equations of the theories applied. At the end of the chapter a description of the numerical models applied are presented.
Chapter 3 and 4 covers the experimental work. In Chapter 3 the incoming waves are described and the surface elevations and velocity fields of the run-up are investigated. The experimental setup for these investigations are given in section 3.2. The investigation of the surface elevation is performed with ultra sonic wave gauges that are placed at different positions at the beach. The positions of the gauges, the results from the measurements and the comparison with the numerical models are presented in section 3.3. To find the velocity fields inside the flow during run-up PIV-technique is used and a description of this technique is introduced in section 3.1, while the different field of views and the results from the measurements and comparison with numerical models are presented in section 3.4. The results from the PIV measurements reveal that there are instabilities in the flow during run-up. Stability of boundary layers are discussed in section 3.4.1.

Chapter 4 covers the tracing of the moving shoreline. In sections 4.1 and 4.2 the experimental setup and the method for postprocessing the data is presented. The results and comparison with the numerical models are given in section 4.3. The tracing of the moving shoreline reveals that the surface tension influences the start of the inundation, and this is further investigated in section 4.3.1 and 4.3.2. Finally, a summary of all the results, the discussion of these and the conclusion is given in Chapter 5.

Chapter 2

Theory

The theory applied in this thesis is potential theory, nonlinear long wave theory and boundary layer theory. In order to find a mathematical description of the flow, it is suitable to divide the flow field into an outer region where the flow is inviscid and an inner region, the boundary layer, which includes the viscosity.

2.1 Lagrangian and Eularian representation

There are two different ways to describe the particle motion in the fluid, Lagrangian and Eulerian representation. Lagrangian representation describes the trajectory of each particle in the fluid, with the particle position $\mathbf{x}$ at a time t as a function of the initial particle position $\mathbf{x}'$ at time t_0. The Eulerian representation describes the whole velocity field. A more detailed description is given in Kundu & Cohen [9]. The most commonly used is the Eulerian representation, although in some cases Lagrangian representation is preferable. Each representation might be transformed into the other. The theory presented in this chapter is two-dimensional flow using the Eulerian representation in a Cartesian coordinate system, while the numerical models for the inviscid flow presented in section 2.7, uses the Lagrangian representation.

2.2 Governing equations

There are two basic equations to describe a fluid flow, namely the Navier-Stokes equation

$$\frac{\partial \mathbf{u}}{\partial t} + (\mathbf{u} \cdot \nabla)\mathbf{u} = -\frac{1}{\rho}\nabla p - \nabla g z + \nu \nabla^2 \mathbf{u} \tag{2.1}$$

and the continuity equation

$$\nabla \cdot \mathbf{u} = 0, \tag{2.2}$$

when $\mathbf{u} = u\mathbf{i} + v\mathbf{j} + w\mathbf{k}$ is the vectorial velocity field, ρ is the density of the fluid, p is the pressure in the fluid, g is the acceleration due to gravity and ν is the

kinematic viscosity of the fluid.
The Navier-Stokes equation describes the conservation of momentum and is valid when the fluid is Newtonian. The continuity equation describes the conservation of mass and is valid as long as the fluid is considered to be incompressible.

2.3 Wave regimes

Gravity water waves are often classified into two separate groups. The waves may be described as either short waves in deep water such as wind generated ocean waves, or long waves in shallow water, such as tidal waves and tsunamis. Short waves on deep water identified as having a small wavelength to depth ratio, $\lambda/d \ll 1$, where λ is the wavelength and d is the depth. When $\lambda/d \gg 1$ the waves are described as long waves in shallow water. The advantage of this classification is that one can neglect terms in the governing equations that turns out to be small due to these assumptions. The waves are also often described as either linear or nonlinear waves, depending on the ratio between the amplitude A and the equilibrium depth d or the amplitude and the wavelength λ. In deep water, waves are considered linear when $A \ll d$. In shallow water, waves are considered linear when $A \ll \lambda$. The linearity simplifies the equations even more.

2.4 Potential theory

One approach to describe the fluid flow field in a run-up is using potential theory. Potential theory is based on the assumption of irrotational motion in an inviscid fluid. In this case, the velocity field $\mathbf{u}$ may be represented as the gradient of a scalar potential, $\mathbf{u} = \nabla\phi$. The advantage of using this representation is its simplicity, as the velocity potential consists of a single scalar unknown from which all three velocity components may be computed. The potential must satisfy the Laplace equation $\nabla^2\phi = 0$, which expresses the conservation of mass and arises from the continuity equation. Together with Bernoulli's pressure equation and boundary conditions, the equations read

$$\nabla^2\phi = 0, \quad 0 < z < \eta \tag{2.3}$$

$$\frac{\partial\eta}{\partial t} + \frac{\partial\phi}{\partial x}\frac{\partial\eta}{\partial x} - \frac{\partial\phi}{\partial z} = 0, \quad z = \eta \tag{2.4}$$

$$\frac{\partial\phi}{\partial t} + \frac{1}{2}(\nabla\phi)^2 + gz = 0, \quad z = \eta \tag{2.5}$$

$$\frac{\partial\phi}{\partial z} = 0, \quad z = -d \tag{2.6}$$

η is the free surface, x is the horizontal axis and z is the vertical axis with $z = d$ at the free surface in equilibrium depth. A more detailed description of the derivation is given in Newman [10].

2.5 Dispersive nonlinear long wave theory

The waves generated in the laboratory are considered to be dispersive nonlinear long waves which means that the nonlinear terms and the deviation from hydrostatic pressure have to be included in the equations.
A classical way to derive a set of equations for the nonlinear long wave problem is described by Gjevik [11]. The approach is to scale the momentum and continuity equations with a typical depth H, a typical wavelength l and a designation for the amplitude α. The long wave parameter ϵ is defined as $\epsilon \equiv \frac{H^2}{l^2}$ and is supposed to be small. The equations are averaged over depth and terms of order ϵ and α are retained while terms of higher order are neglected. This leads to the well known boussinesq equations

$$\bar{u}_t + \eta_x + \alpha\bar{u}\bar{u}_x - \epsilon[\frac{h}{2}(h\bar{u})_{xxt} - \frac{h^2}{6}\bar{u}_{xxt}] + O(\epsilon^2, \alpha\epsilon) = 0 \tag{2.7}$$

$$\eta_t + (h\bar{u})_x + \alpha(\eta\bar{u})_x = 0 \tag{2.8}$$

where $\overline{u} = \frac{1}{h+\alpha\eta}\int_{-h}^{\alpha\eta} u dz$ is the horizontal velocity component averaged over depth, and η is the surface elevation.
These equations are valid for variable depth, include dispersion and nonlinearity and can be solved numerically with proper boundary conditions.
The Lagrangian long wave model presented in section 2.7 differs from equations (2.7) and (2.8) in the sense the the equations are fully nonlinear and include terms of order $O(\alpha\epsilon)$, see Jensen *et al* [5].
In particular cases, nonlinearity and deviation from hydrostatic pressure are of the same order, and the tendency to wave breaking due to nonlinearity and dispersion due to the non-hydrostatic pressure counterbalance each other. The wave occurring is nonlinear long waves with constant velocity and unchanged shape, so called Solitary waves.

2.6 Boundary layer theory

Close to the beach, the fluid viscosity can not be neglected and at the beach there is full adhesion. This will affect the velocity field and thus influence the maximum run-up height. The use of the laminar boundary-layer equations are a celebrated approach to this problem, as described by White [12]. In the derivation of the laminar boundary layer equations a flow with free stream velocity $\mathbf{U} = U\mathbf{i}$ passes a thin body of length L is considered. Assuming that the boundary layer is laminar and that the Reynolds number $Re = \frac{UL}{\nu}$ is high, there exists a thin boundary layer near the beach. The first step to the solution is to scale the momentum- and continuity equation with $x^* = \frac{x}{L}$, $z^* = \frac{z}{L}\sqrt{Re}$, $t^* = t\frac{U}{L}$, $u^* = \frac{u}{U}$, $w^* = \frac{w}{U}\sqrt{Re}$ and $p^* = \frac{p-p_0}{\rho U^2}$, where * denotes dimensionless variables. Evaluting the governing equations and assuming that the Reynolds number is large the

laminar boundary layer equations reads:
Continuity equation:

$$\frac{\partial u^*}{\partial x^*} + \frac{\partial w^*}{\partial z^*} = 0 \tag{2.9}$$

x-component momentum equation:

$$\frac{\partial u^*}{\partial t^*} + u^*\frac{\partial u^*}{\partial x^*} + w^*\frac{\partial u^*}{\partial z^*} = -\frac{\partial p^*}{\partial x^*} + \frac{\partial^2 u^*}{\partial z^{*2}} \tag{2.10}$$

z-component momentum equation:

$$0 = \frac{\partial p^*}{\partial z^*} \tag{2.11}$$

As seen from equation 2.11, the pressure distribution is uniform across the boundary layer, and the pressure distribution in the outer, inviscid flow can be used in the boundary layer. The expression for the pressure field is found from Eulers' pressure equation and reads

$$-\frac{\partial p^*}{\partial x^*} = \left[\frac{\partial U^*}{\partial t^*} + U^*\frac{\partial U^*}{\partial x^*}\right]_{z=0}, \tag{2.12}$$

when $U^* = \frac{U(x,t)}{\sqrt{gH}}$. In addition to the pressure distribution, we need to match the outer solution with the boundary layer solution which gives us the boundary condition $u(x, z \to \infty, t) \to U(x, t)$. Together with the non-slip condition at the bottom and proper initial and inlet conditions, the equations can be solved. These equations are valid as long as the Reynolds number is large, but when the Reynolds number becomes too large, (typically $O(10^5)$), the laminar solutions becomes unstable and transition to turbulence occurs.

2.7 Numerical models

There are two different models applied to the investigation of the outer region in the solitary wave run-up problem. One is the Lagrangian long wave model and the other is the boundary integral model. The models are based on inviscid theory and Lagrangian description of the fluid flow. The advantage of the Lagrangian description is that the boundary conditions at the moving shoreline becomes easier to implement.
The theory applied for the Lagrangian long wave model is a version of the Boussinesq equations that are fully nonlinear but have only standard dispersion properties. A detailed description of this model is presented in Pedersen & Gjevik [1], Jensen *et al.* [5] and Pedersen [13].
The boundary integral model (BIM) is based on full potential theory, and solves the Laplaces equation with a free surface. A detailed description of the model

is given in Appendix A, and the model is also presented and tested in Pedersen [14].
The boundary layer model is nonlinear and uses the velocities found from the BIM or Boussinesq model as a boundary condition. A detailed description of the model for the boundary layer is given in Appendix B, where the model also is tested.

Chapter 3

Surface elevations and velocity fields

To be able to conclude what causes the reduced run up height there are three different aspects of the flow investigated, the surface elevation, the velocity field and finally the moving shoreline. They all have the same incoming solitary wave, but otherwise they are independent of each other. The solitary waves are characterized by their amplitude and in total there are five different waves generated, A/d = [0.0977, 0.195, 0.292, 0.388, 0.481], where d is the equilibrium depth and A is the amplitude of the incoming wave. Hereafter, these will be referred to as case 10, 20, 30, 40 and 50, and are visiualized in figure 3.1. None of the waves show any sign of breaking.
In this chapter, the investigations of surface elevation and velocity field using well known methods are presented. The tracing of the moving shoreline has not, known the the author, been done before and is presented in chapter 4. In all experiments there are three runs performed, and the data is averaged. The two reasons for doing this is, firstly to make sure that the repeatability of the incoming waves is satisfying and secondly, averaging the data smooths out unwanted noise. The results from the experiments is compared with theory for case 10, 20 and 30. The numerical models do not cover case 40 and 50.

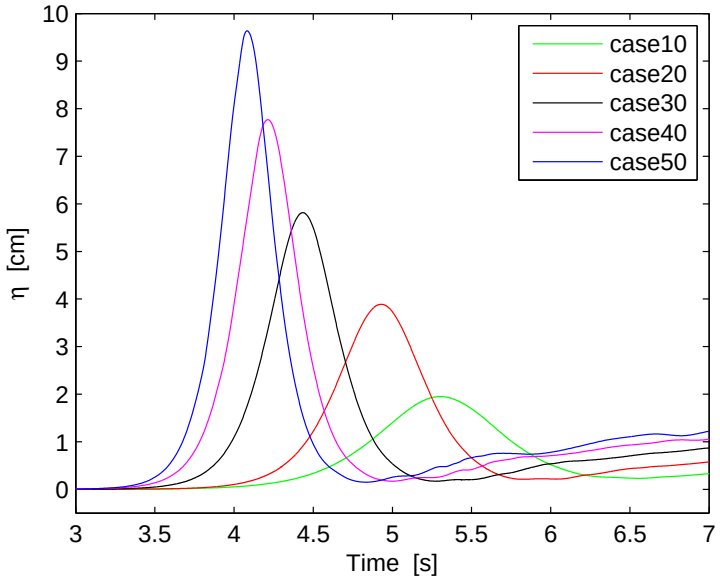

Figure 3.1: Incoming solitary waves, measured at x=-2.045 m

3.1 Particle image velocimetry (PIV)

Particle image velocimetry is a commonly used method in the experimental investigation of fluid dynamics. The fluid is seeded with neutrally buoyant tracer particles with the assumption that the particles will follow the flow. Velocities are determined by taking two images separated by the timestep Δt. The displacement Δx of the particles during Δt is measured and the velocity is calculated by $\mathbf{u} = \frac{\Delta x}{\Delta t}$.
PIV measurements requires a light source, usually a pulsed laser, that is shaped with an optical device into a two dimensional light sheet. The measurements also requires a recording device, usually a digital camera, which collects images of the particles as they pass through the light sheet.
There are two typical implementations of PIV: Single exposure multiple image and multi exposure single image. An autocorrelation technique is used to determine the velocities in multi exposed single images, while a cross-correlation technique is used for the single exposed multiple images. Cross-correlation is more accurate and is the one that will be discussed in this section.
In order to find the velocity in the field of view (FOV), cross correlation between two images is performed. The first step to this analysis is to divide the images of size X×Y pixels into two interrogation windows of size M×N pixels, with several particles in each interrogation window. When this is done, a cross correlation beetween the two interrogation window pair in the image pair is performed. The cross correlation function is defined as (see Sveen and Cowen [15])

$$R(s,t) = \frac{1}{N^2} \sum_{i=0}^{N-1} \sum_{j=0}^{N-1} F'_{I,J}(i,j) F''_{I,J}(i+s, j+t), \tag{3.1}$$

When F' is the first image of the image pair, and F'' is the second, $F'_{I,J}$ is the interrogation window considered in the first image and $F''_{I,J}$ is the corresponding interrogation in the second image, i, j is the pixel location within subwindow and s, t is the lag at which the cross-correlation is being computed.
The result is a correlation plane, which consists of three different contributions, namely the correlation of the mean background intensities, correlation of the mean and the fluctuating intensities and correlation of the fluctuating intensities. It is the last mentioned that contains the displacement peak which also is the highest, and the others are considered as noise. The ratio between the displacement peak and the rest of the plane will provide information about the signal to noise ratio.
In order to evaluate the degree of match between the interrogation window patterns, and the signal to noise ratio, the correlation calculated in equation (3.1) needs to be normalized, the normalized cross covariance function is defined as

(see Sveen and Cowen [15])

$$\bar{R}(s,t) = \frac{1}{N^2} \frac{\sum_i \sum_j [F'(i,j) - \bar{F}'][F''(i+s, j+t) - \bar{F}'']^2}{\sum_i \sum_j ([F'(i,j) - \bar{F}']^2 [F''(i+s, j+t) - \bar{F}'']^2)^{1/2}} \tag{3.2}$$

When $\bar{F}' = \text{mean}(F(i,j))$ and $\bar{F}'' = \text{mean}(F''(i+s, j+t))$. After the normalization, the height of the correlation peak is a good measurement of the quality of the correlation. The value will be in the range 0 to 1, with 1 indicating a very high degree of match between the interrogation windows.
One important thing to notice is that if the displacement is larger than N/2 pixels, the correlation peak will alias the location $-(N - \xi)$ where ξ is the actual displacement. If the displacement is bigger than N, the correlation peak will be the result of two uncorrelated interrogation windows, and thus will be a random noise peak.
Since the correlation peak is larger than one pixel [15], it is useful to be able to determine the correlation peak in sub-pixel position to avoid peak-locking. A three-point sub-pixel estimation are generally sufficient. There exists several estimators, but the most commonly used is Gaussian fit, which performs best with all particle diameters. Another approach to avoid peak-locking is to use continuous windowshift, which means that one dynamically shift the interrogation window until the subpixel displacement is identically zero.
The resulting velocity field will contain spurious vectors, that need to be detected and excluded from the result. There are three fundamental approaches to validate the vectors, Signal-to-noise ratio filtering, global filtering and local median filtering. The signal-to-noise ratio filtering is done by simply determine a threshold value of the ratio between the first correlation peak (signal) to the second correlation peak (noise). Usually, this threshold value is in the range of 1.2 to 1.5. The global mean filtering means that one compare one singel vector, with the whole ensemble of vectors in the field. If the vector considered is "very" different from the mean of the whole ensemble, it is considered to be an outlier. In the local median filtering the vector is compared with the median of its closest neighbors and excluded if it is "very" different. The deviation accepted in the global and local filter is determined by the user with a threshold value.
More detailed descriptions of the PIV technique are found in Sveen & Cowen [15] and M. Raffel *et al* [16].

3.2 Experimental setup

The experimental work is done in the wave tank at the Hydrodynamics Laboratory at the University of Oslo. The tank is 25 m long, 0.5 m wide and 1 m deep. The tank walls and bottom are made of glass. The beach is mounted 5.97 m from the wave paddle, and the beach/still water intersection is located 7.10 m from the paddle. A schematic view of the beach is shown in figure 3.2. The wave paddle is a vertical piston type, the wave generation procedure is explained in Jensen *et al* [5].
Two coordinate systems are introduced. Firstly, a (x,y)-coordinate system with x-axis in horizontal direction and x=0 at the beach/still water intersection and the y-axis in vertical direction with y=0 at the still water level is introduced. Secondly, a (s,z)-coordinate system with s-axis parallel to the beach with s=0 at the beach/still water intersection and z-axis orthogonal to the beach with z=0 at the beach. The water depth is 20.0 cm in all experiments. The beach has an angle of inclination of $\theta = 10°$ and is made of PETG.
The beach is slightly deformed perpendicular to the traveling direction of the flow. It is concave between s=0 m and s= 0.70 m, with a discrepancy of 0.10 mm to 1.45 mm, and the maximum discrepancy is located at s=0.80 m. It is convex between s=0.90 m and s=2.30 m, with a discrepancy of 0.1 mm to 0.4 mm, and the maximum discrepancy is located at s=2.30 m. In addition, the beach is deflected during the inundation due to the weight of the water, and this is most pronounced at the lower end of the beach. The maximum deflection recorded is 1.4 mm in FOV1 for case 50.
The surface elevation is measured by non-intrusive ultrasonic wave gauges (Ban-

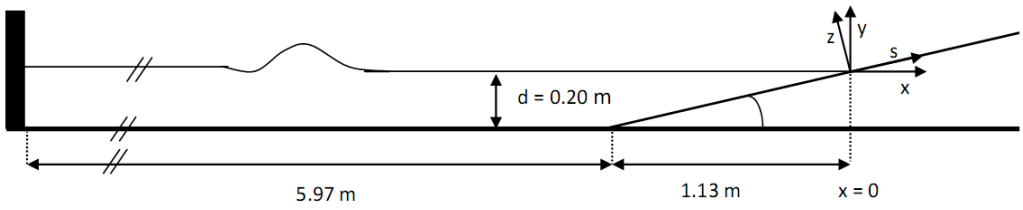

Figure 3.2: Schematic side view of the wavetank

ner U-Gage S18). The concept of this type of gauges is that the ultrasonic sensors emit one or multiple pulses of ultrasonic energy, which travel through the air at the speed of sound. A portion of this energy reflects off the target and travels back to the sensor. The sensor measures the total time required for the energy to reach the target and return to the sensor. The distance D to the surface is then calculated from D = ct/2 where c is the speed of sound in air and t is the transit time for the ultrasonic pulse. The sensing range is from 30 mm to 300 mm, with a maximum angle to the target of 10^o, and outside this range the results are not

reliable. The accuracy is about 1/10 of a mm when the sensor are vertical to the surface, the accuracy decreases with increasing angle and when the angle is 10 degrees the accuracy of the gauges is about 1 mm. The accuracy of the gauges are carefully checked, presented in Appendix C. In all, four gauges are used set to sample at 200 Hz.

The recording device for PIV is a Photron SA5 with a 1024×1024 pixels resolution and a framerate of 2000-5000 fps, depending of the celerity of the incoming wave. Tracer particles are 50 μm polyamid spheres. As light source, a Quantronix Darwin Duo pulsed laser giving 15 mJ energy output at 3000 Hz. The camera was located outside the tank, parallel to the beach. The laser was located underneath the tank creating a light sheet oriented tangentially to the traveling direction of the flow.
To be able to compare the experimental results with theory, both the gauges and the PIV system where synchronized with the paddle using a trigger system with t=0 at the paddle start.

3.3 Surface elevation, measurements and results

There are four ultra sonic wave gauges used in the investigation of the surface elevation. One gauge is placed in the deep water region and is used to control the quality of the incoming wave, control the equilibrium depth and as input for the numerical models. The other three gauges are placed at different positions at the beach. Gauge 2 is placed near the beach/still water intersection while gauge 3 and 4 are placed further up the beach.
Since the validity range and accuracy of the gauges are limited by the angle to the target, the position of the gauges are carefully evaluated with respect to the shape of the wave at the thought gauge position. This evaluation is made by using results from numerical simulations of case 10, 20 and 30 and doing a visual inspection of how the incoming wave evolves with time at the thought position. The simulations reveals that the run up tongue becomes thin and nearly parallel to the beach further up the beach as vizualised in figure 3.3. On this basis, Gauge 1 and 2 where placed perpendicular to the free surface, while gauge 3 and 4 where placed perpendicular to the beach. The positions of the gauges reads x = [-2.045 m, 0.149 m, 0.353 m, 0.623 m], where x=0 is at the beach/still water intersection. A schematic view of the gauges positions is shown in figure 3.4

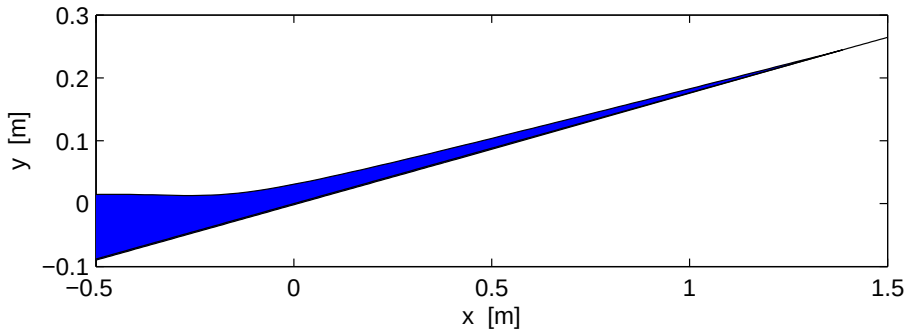

Figure 3.3: Surface profile for case 30 at maximum inundation (BIM)

There are drop outs in the data due to steepness of the incoming waves. Those areas are interpolated with linear interpolation, also the data from the gauges are filtered with a Savitzky-Golay filter to exclude noise. The software used for the interpolation and the filtering is matlab. The raw data and the result from filtering and interpolation for case 50 is shown in figure 3.5.

The results are presented in figure 3.6-3.10. As seen in figure 3.6, 3.7 and 3.8 Case 10, 20 and 30 have excellent agreement with the boundary integral model (BIM) and the Boussinesq model (Bouss) for the incoming wave at at the position of gauge 1, even though the Boussinesq model reveals some distortions at the tail. At the position of gauge 2, 3 and 4 the models do not give the same results,

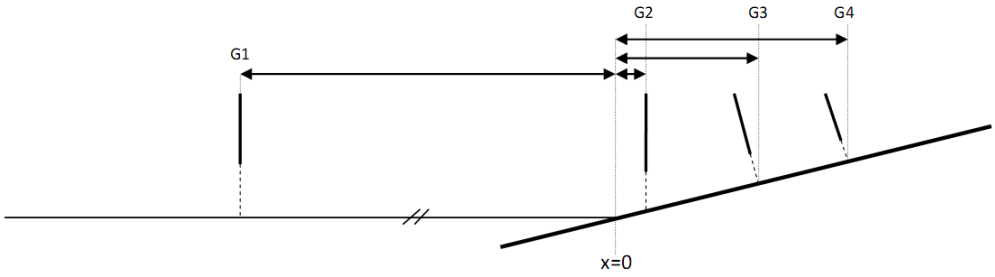

Figure 3.4: Schematic side view of the ultra sonic gauges positions

the Boussinesq-model have a higher surface elevation than the boundary integral model, and the deviation increases with the amplitude of the incoming wave.
For case 10, figure 3.6, both the time and amplitude in the experimental results shows very good agreement with theory at the position of gauge 2. Further up the beach, the wave does not reach gauge 3.
For case 20, figure 3.7, both the time and amplitude shows very good agreement between the BIM model and the experimental results at the position of gauge 2 and 3. At the position of gauge 4 on the other hand, the amplitude match of the experimental result is best with the Boussinesq model and the models are ahead the wave considering the time.
For case 30, figure 3.8, both the time and amplitude shows good agreement between the BIM model and the experiment at all gauge positions.
From these results, it seems like the theory and the experiments agree well in the start of the inundation, and the discrepancies are more pronounced in the later stage of the run-up considering the surface elevation.

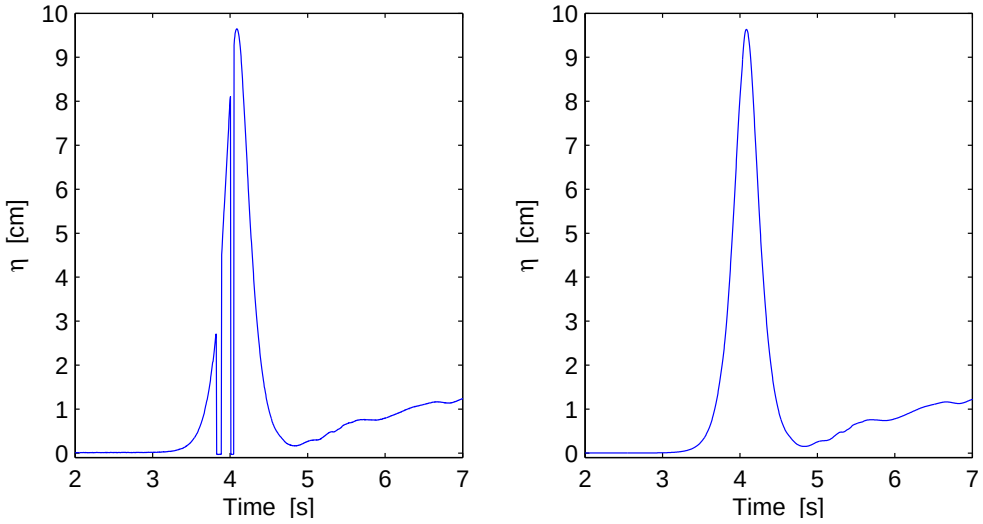

Figure 3.5: Case 50, Gauge 1. Left: Raw data. Right: The data is interpolated and filtered.

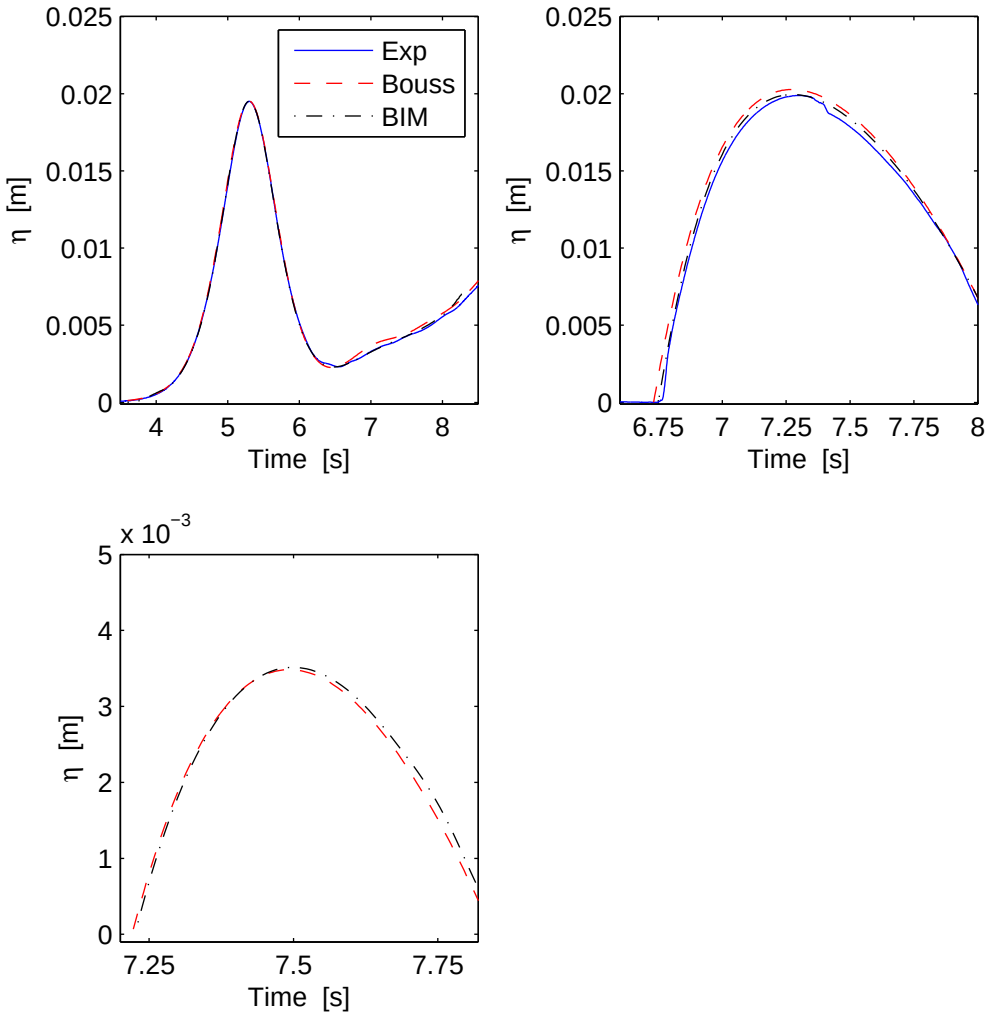

Figure 3.6: Case 10. Upper left: Gauge 1, Upper right: Gauge 2, Lower left: Gauge 3

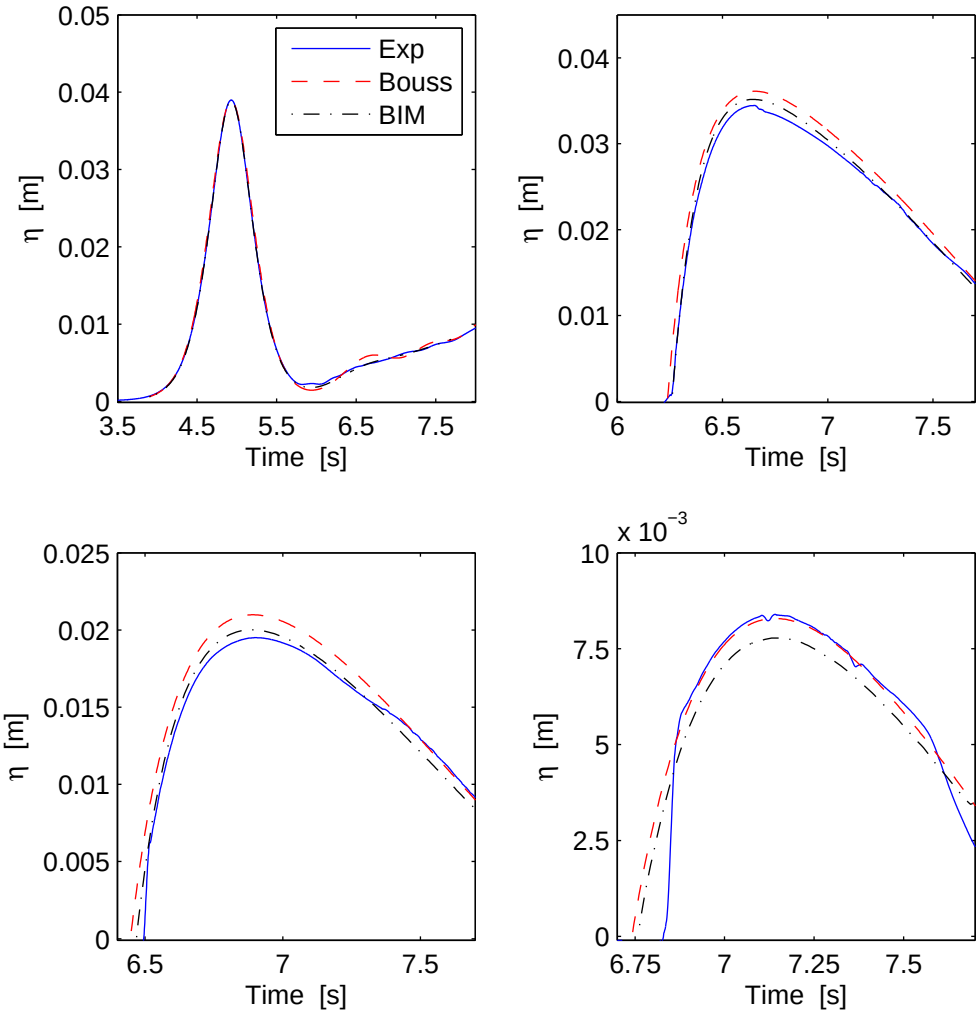

Figure 3.7: Case 20. Upper left: Gauge 1, Upper right: Gauge 2, Lower left: Gauge 3, Lower right: Gauge 4

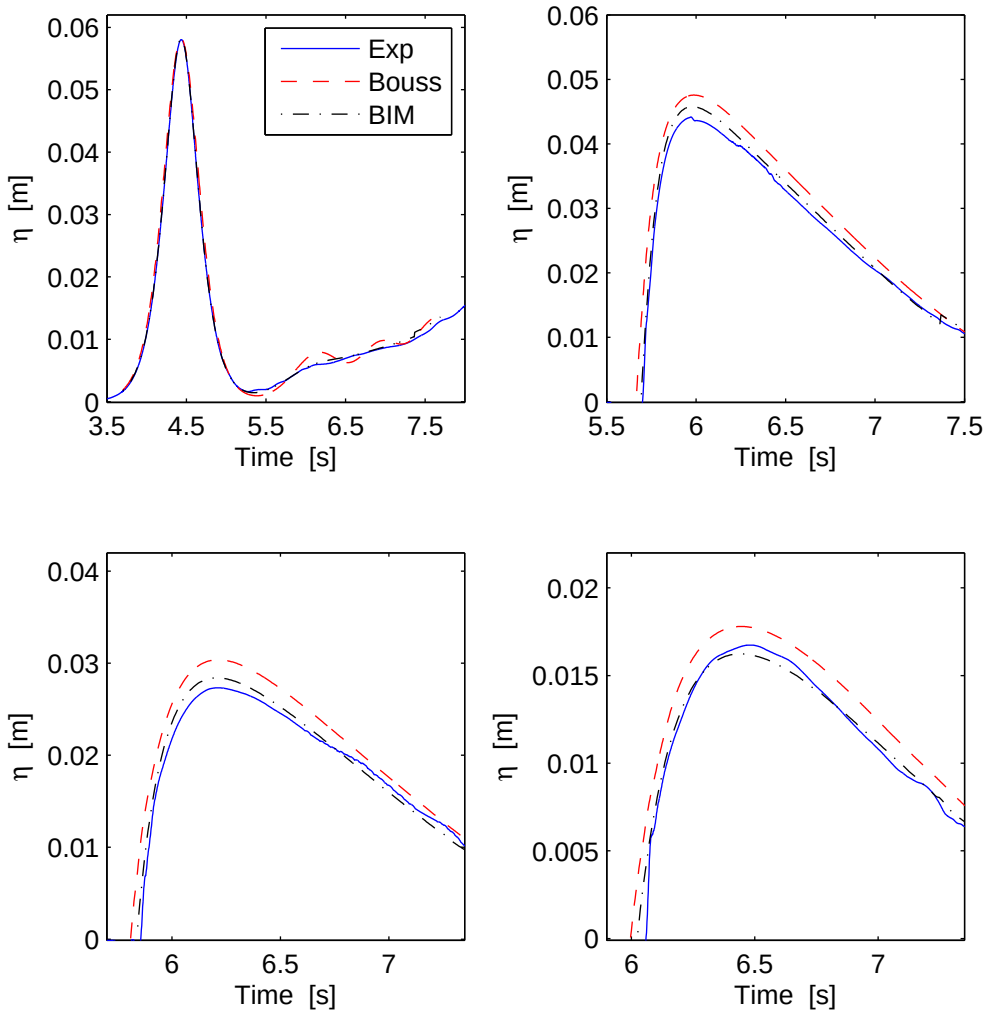

Figure 3.8: Case 30. Upper left: Gauge 1, Upper right: Gauge 2, Lower left: Gauge 3, Lower right: Gauge 4

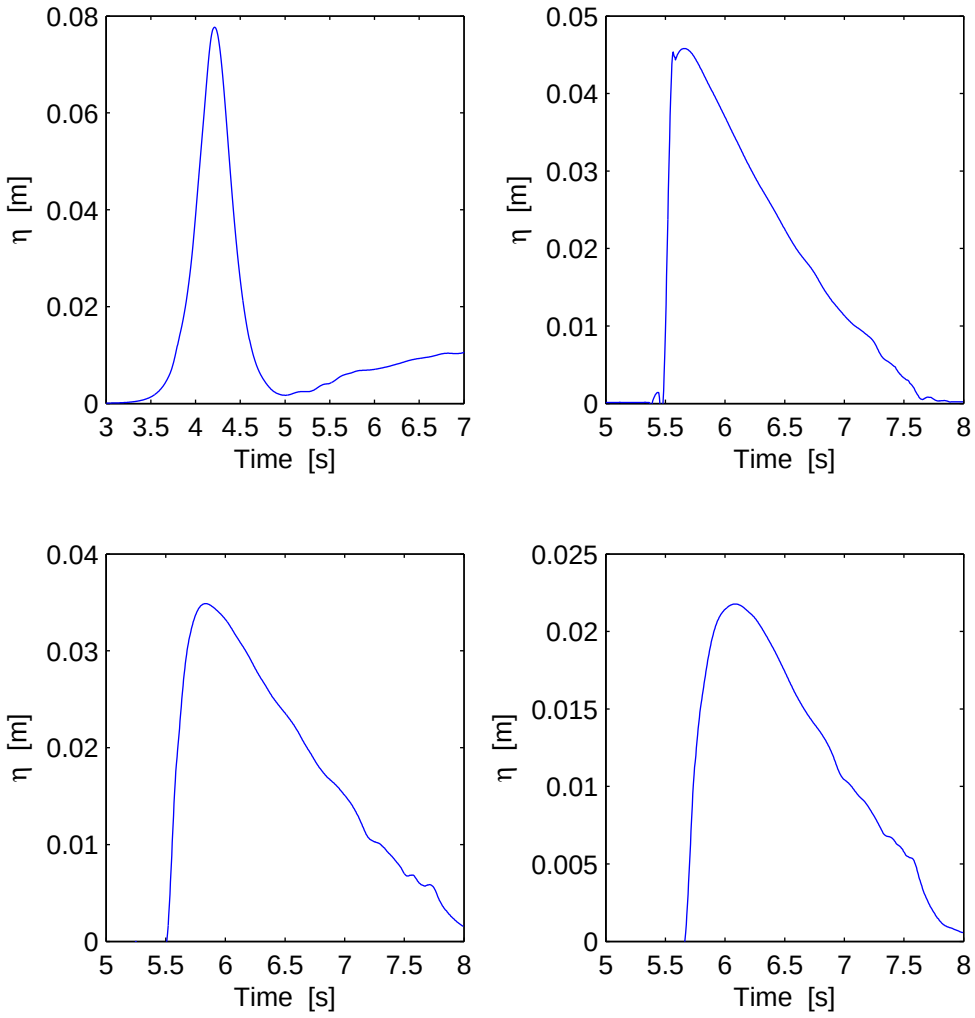

Figure 3.9: Case 40. Upper left: Gauge 1, Upper right: Gauge 2, Lower left: Gauge 3, Lower right: Gauge 4

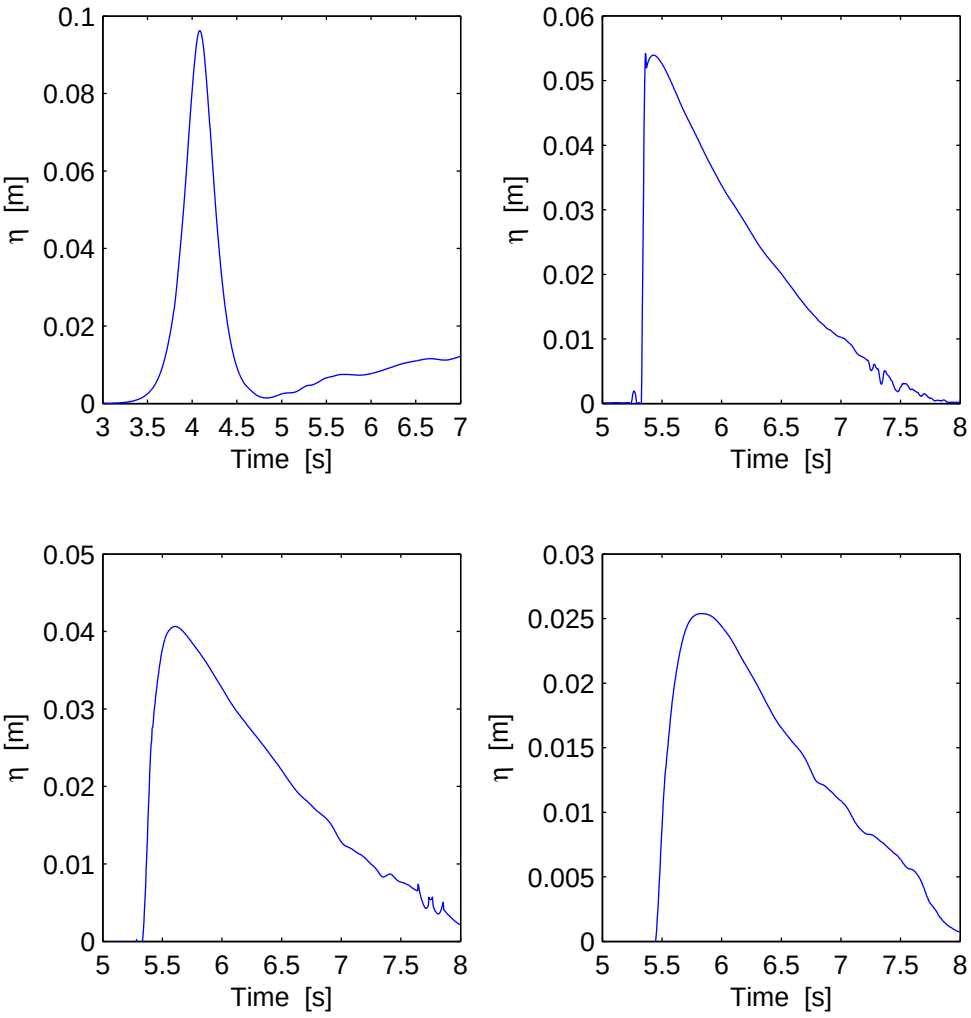

Figure 3.10: Case 50. Upper left: Gauge 1, Upper right: Gauge 2, Lower left: Gauge 3, Lower right: Gauge 4

3.4 PIV measurements and results

There are three different field of views (FOV) considered, herafter referred to as FOV 1, 2 and 3. FOV 1 is 5.6×5.6 cm with center of the image located at s=0.082 m and the light sheet (focal area) is in the middle of the tank. FOV 2 is 2.3×2.3 cm with center of the image located at s=0.075 m and the light sheet is located 5 cm from the wall closest to the camera. FOV 3 is 3.3×3.3 cm with center of the image located at s=0.81 m and the light sheet located 5 cm from the wall closest to the camera.
Digilow was used for the image processing, see Dalziel [17], and the size of the interrogation window was 32×8 pixels with 50% overlap. The size of the interrogation window is chosen is based on the assumption that the variations in velocities are larger in the vertical direction than in the horizontal direction. This is why we need a finer resolution in the vertical direction. In the postprossesing, between 5% and 25% of the calculated vectors where rejected, and the results are considered reliable.
To be able to transform the pixel coordinates to the world coordinates, a coordinate system is recorded in the start of each experiment. Due to deflection of the beach in FOV1, the coordinate system is time-dependent and the coordinate system is recorded during the whole inundation. FOV1 is mainly used as a safety check to the results from FOV2.
In the laminar regime the data from three runs over an Δs is averaged to smooth the data. In the unstable regime, no smoothing is applied.

The model for the outer inviscid fluid that is used as boundary condition for the computation of the boundary layer is the BIM model. The Boussinesq model shows good agreement with the experiments for case 10 but for case 20 and 30 deviation from both the experiments and the BIM model is revealed.

As seen in figure 3.11-3.15 there is a well defined laminar boundary layer with thickness 3-4 mm close to the beach for all cases in FOV2. The apperance of a boundary layer will cause a reduced onshore volume flux during inundation in comparison with inviscid theory. The thickness of the boundary layer and the shape of the boundary layer agrees well with the theory for case 10, 20 and 30. Considering the outer flow, there are discrepancies between experiment and theory. The outer velocities in the theoretical result are smaller than the outer velocities in the experimental results, and it seems like the theoretical results are ahead of the experimental results with respect to the time. This deviation is decreasing with time, see figure 3.16-3.18.
The flow inside the boundary layer reverses before the outer flow does, in the same manner as observed by Liu *et al* [7] underneath a solitary wave propagating on constant depth. The early flow reversal in the boundary layer is visualized in figure 3.12 at t=6.9 s, where it is clear that the outer flow still is moving in the

positive s-direction, while the boundary layer has started the reversal. Sælevik [6] found the same phenomena in his study of run-up of solitary waves and suggested the the early reversal in the boundary layer was caused by the gravity acting at the fluid with low velocity due to to the non-slip condition at the beach boundary. The flow reversal in the boundary layer will affect the flow in the sense that the z-component of the velocity will increase in the negative z-direction and this will cause draining effects on the flow.

There are instabilities in the boundary layer during the run-up for case 30, 40 and 50, showing what might appear to be a transition to turbulence. This assumption is based on visual observation from the PIV-recordings.
Case 50 is very unstable, and in some of the runs in FOV1 there is a clear tendency of turbulence, which has not been observed in FOV2. The instabilities in FOV1 might be induced by the deflection of the beach during inundation which demonstrates how labile the flow is. An example of this instabilities i illustrated in figure 3.19, where the velocity field is plotted at the same time instant for two different runs.
In FOV3, the visual inspection reveals instabilities in case 30, 40 and 50. These instabilities seems to be generated inside the boundary layer and is spreading to the outer flow. Velocity profiles of case 30 in FOV 3 is shown in figure 3.20 and the boundary layer is not well defined.
The z-component of the velocity field also yields some information of the stability in the flow. Figure 3.21 shows the z-component of case 30 in FOV2, where the flow is laminar. The experimental results agrees well with the theory, even though there are some discrepancy at t=5.7s. Figure 3.22 shows the z-component of the velocity in FOV3 where it is clear that the flow is unstable, with both positive and negative velocities. The positive velocities are unexpected and would not appear in a laminar flow. These fluctuations in the z-component of the velocity is also found in case 40 and 50, case 50 is visualized in figure 3.23.

An interesting observation is that the boundary layer for case 30, 40 and 50 is laminar in FOV2 during both run-up and run-down while instabilities are recorded in FOV3. This means that the flow is stabilizing during run-down and the boundary layer again becomes stable and laminar before it reaches FOV2.

3.4.1 Stability of boundary layers

In the discussion of stability of laminar boundary layers, the Reynolds number in the flow is an essential parameter. The Reynolds number is defined $Re \equiv Ul/\nu$, where U is the characteristic velocity in the flow and l is the characteristic length scale. If the Reynolds number of the outer flow is larger than a critical Reynolds number, Re_C, the boundary solutions become unstable and transition to turbulence occurs.

In order to find a critical Reynolds number for the run-up of solitary waves, we need to look for similar investigations found in the literature. The Falkner-Skan wedge-flow described by White [12] investigates a constant outer flow passing a wedge, which is similar to the run-up of solitary waves in the sense that the outer flow is non-parallel to the wall, or in our case the beach. The Falkner-Scan wedge-flow has a critical Reynolds number $Re_{Cfs} = 5.4 \times 10^4$. One should keep in mind that the Falkner-Scan wedge-flow solution does not include gravity, and that in the run-up of solitary waves the outer flow is transient.
Sumer *et al* (2010) [18] investigated the boundary layer under solitary waves propagating on constant depth. They defined the Reynolds number $Re = (aU_{0m}/\nu)$ where a is half of the stroke of the water particle displacement in the outer flow and U_{0m} is the horizontal velocity in the outer flow. They report a critical Reynolds number of $Re_{Csw} = 5 \times 10^5$. In this case the outer flow is transient, but the depth is constant.
It is reasonable to expect that the critical Reynolds number in our case is within the range of Re_{Cfs} and Re_{Csw}.

To find the Reynolds numbers in the solitary waves generated in the laboratory, an estimation of l and U is needed. For l it is natural to use the x-component of the maximum inundation length, which results in $l_x = Rcot\theta$, where R is the maximum run-up height and θ is the angle of the beach. U is approximated by the assumption that the flow is dominated by gravity and given as $U = \sqrt{2gR}$. The run-up heights are given in chapter 4. This gives Reynolds number

$$Re = \frac{\sqrt{2gR}Rcot\theta}{\nu} \tag{3.3}$$

Equation 3.3 gives the specific Reynolds numbers given in table 3.1. One should keep in mind that these Reynolds numbers are roughly estimated, but they reveal that the generated waves are in a critical regime.

Case	Re
10	3.68×10^5
20	1.19×10^6
30	2.27×10^6
40	3.57×10^6
50	4.97×10^6

Table 3.1: Reynold numbers of the solitary waves

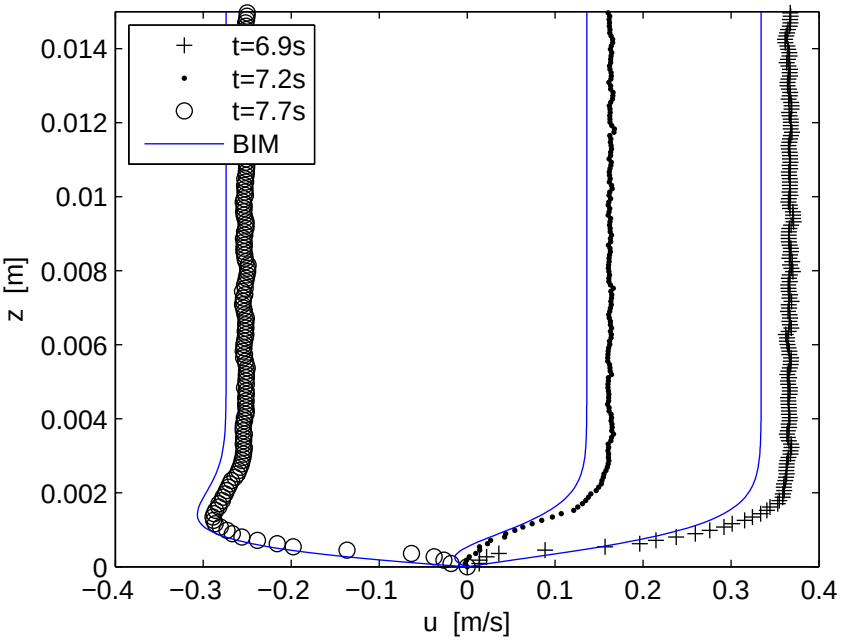

Figure 3.11: Velocity profiles of u for case 10 FOV2, averaged over Δs=0.5 cm from s=0.065 m to s=0.070 m

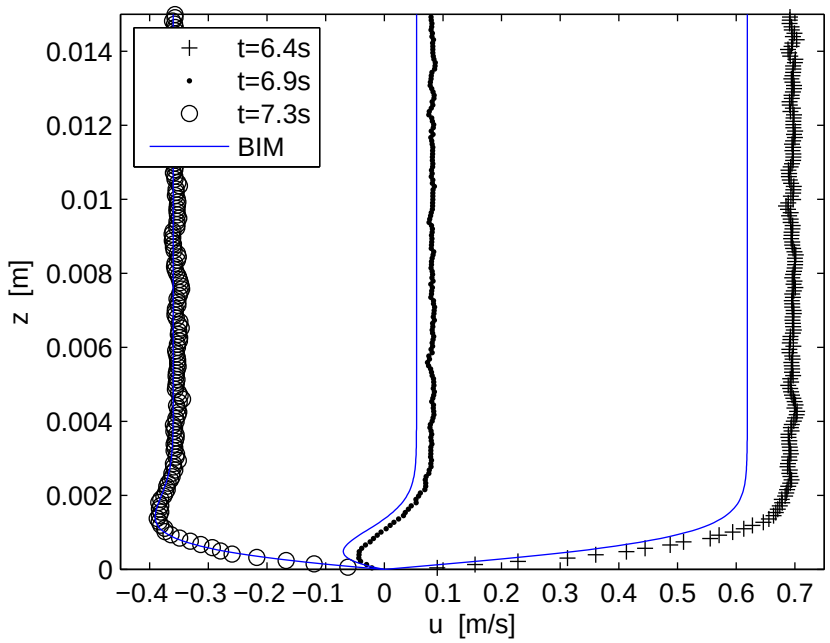

Figure 3.12: Velocity profiles of u for case 20 FOV2, averaged over Δs=0.5 cm from s=0.064 cm to s=0.069 m

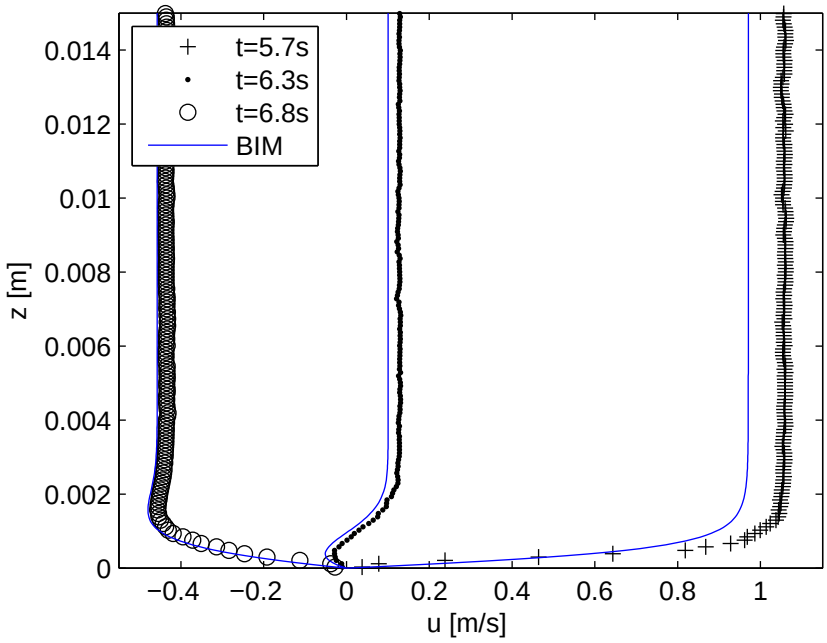

Figure 3.13: Velocity profiles of u for case 30 FOV2, averaged over Δs=0.4 cm from s=0.065 cm to s=0.069 m

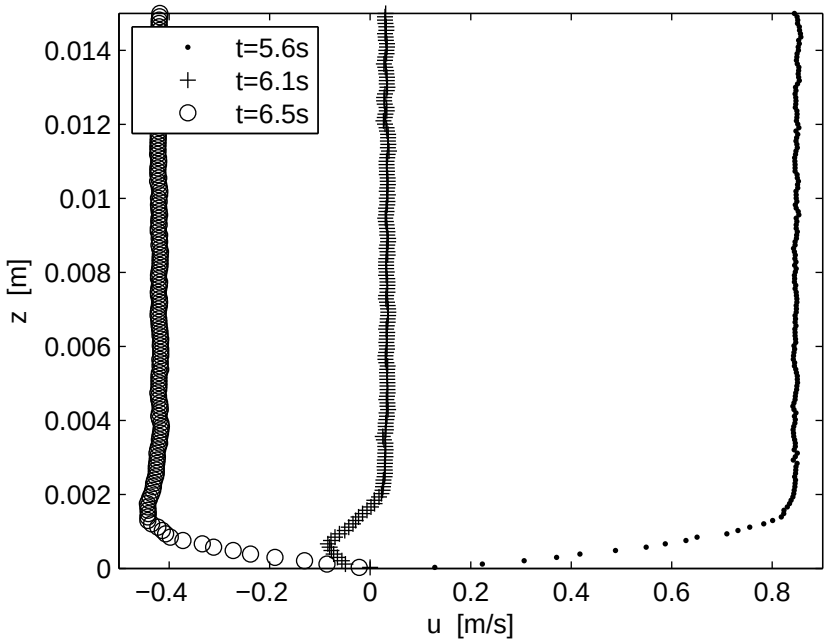

Figure 3.14: Velocity profiles of u for case 40 FOV2, averaged over Δs=0.5 cm from s=0.065 m to s=0.070 m

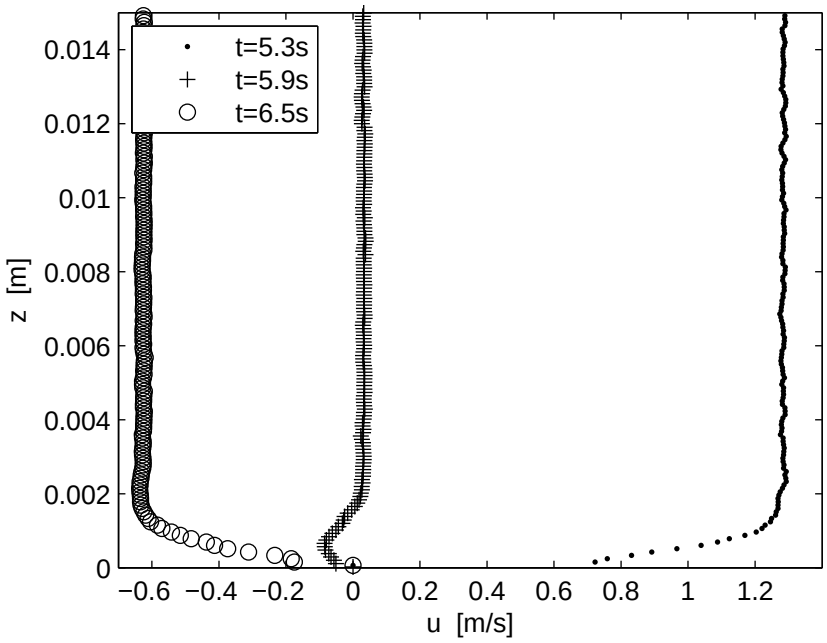

Figure 3.15: Velocity profiles of u for case 50 FOV2, averaged over Δs=0.5 cm from s=0.065 m to s=0.070 m

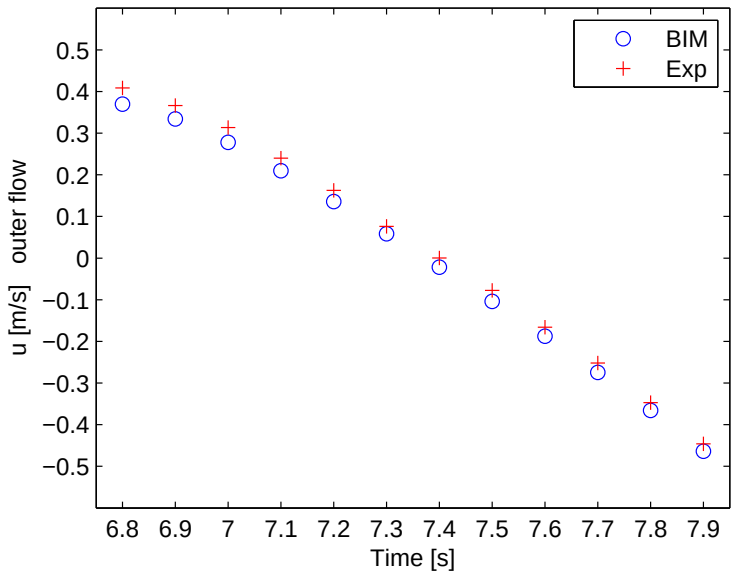

Figure 3.16: Case 10, Outer velocity FOV2

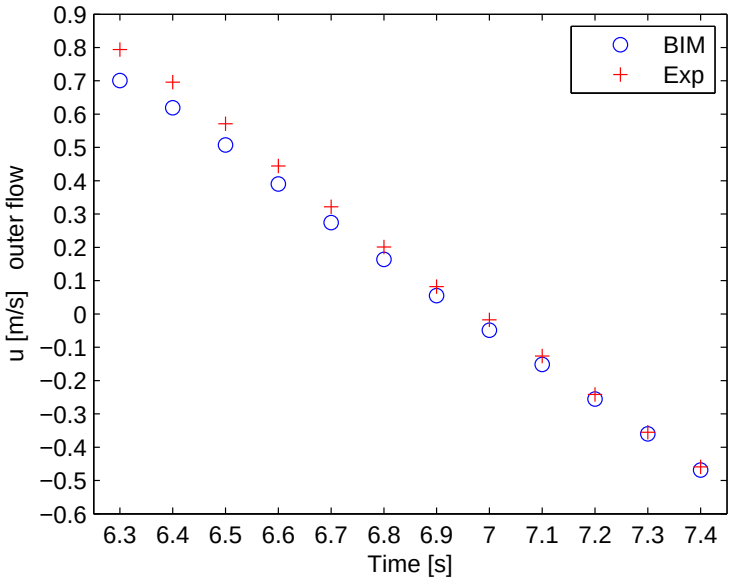

Figure 3.17: Case 20, Outer velocity FOV2

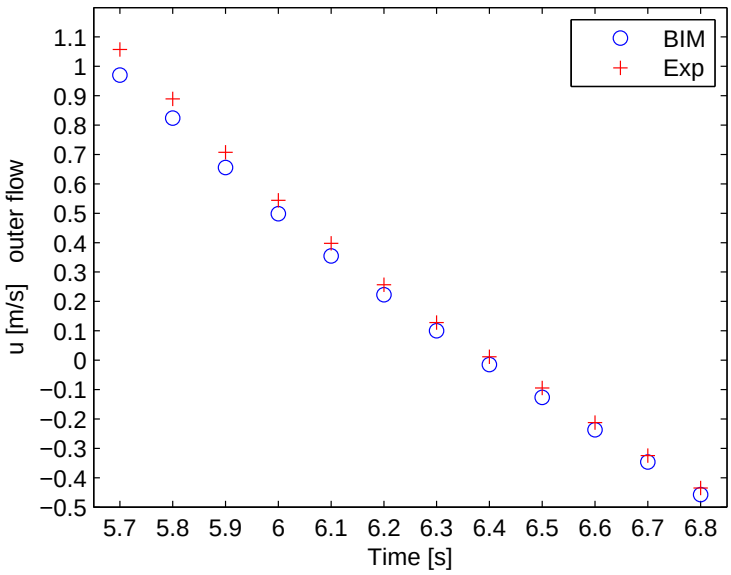

Figure 3.18: Case 30, Outer velocity FOV2

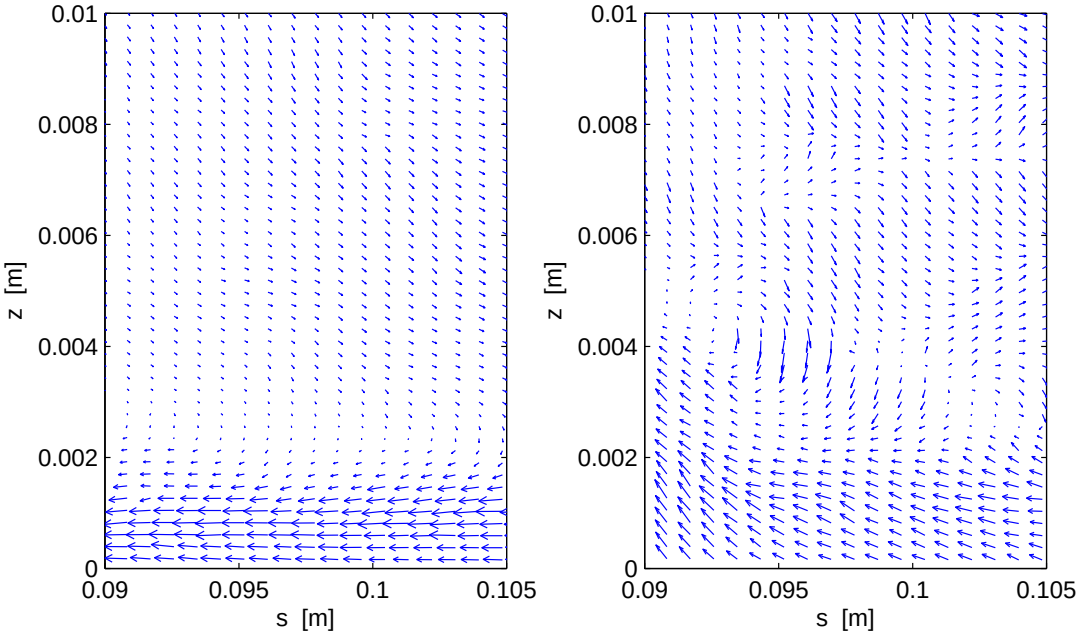

Figure 3.19: Velocity fields in FOV 1 case 50, at time 6.0 s. Right: Run 1, Left: Run 2

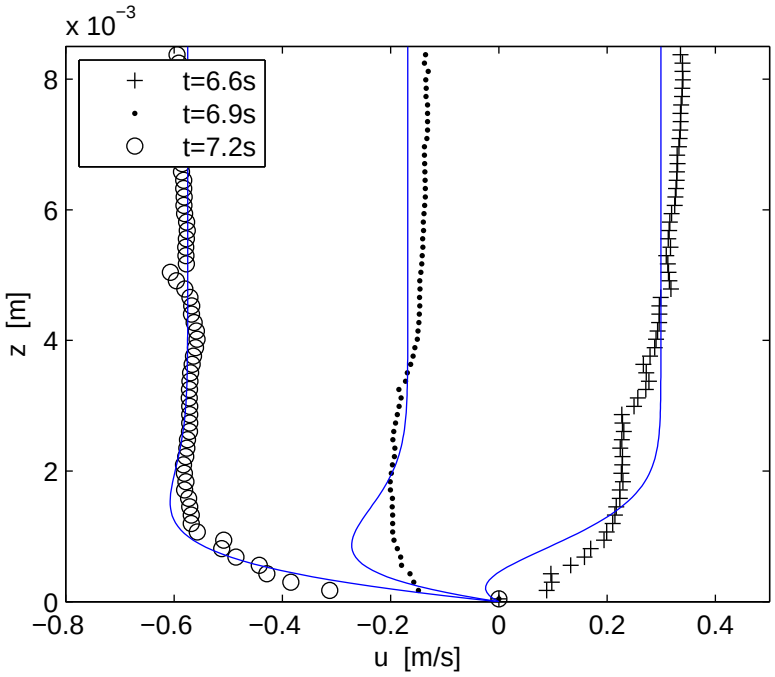

Figure 3.20: Velocity profiles of u for case 30 FOV3, at s=0.803 m

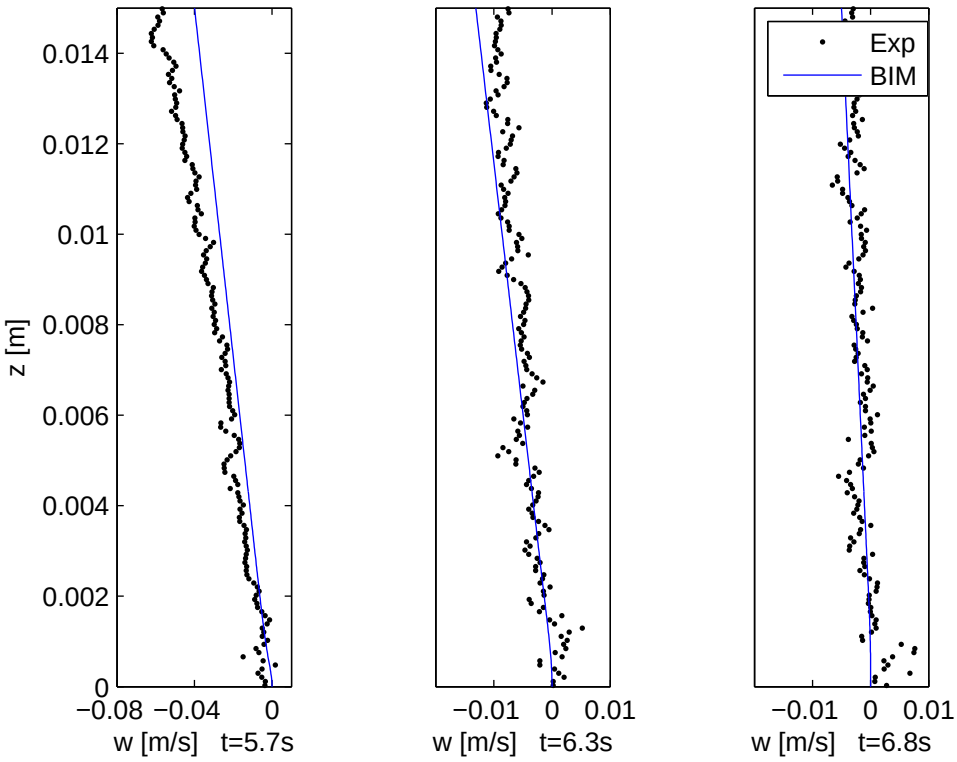

Figure 3.21: Velocity profiles of w for case 30 FOV2, averaged over Δs=0.4 cm from s=0.065 m to s=0.069 m

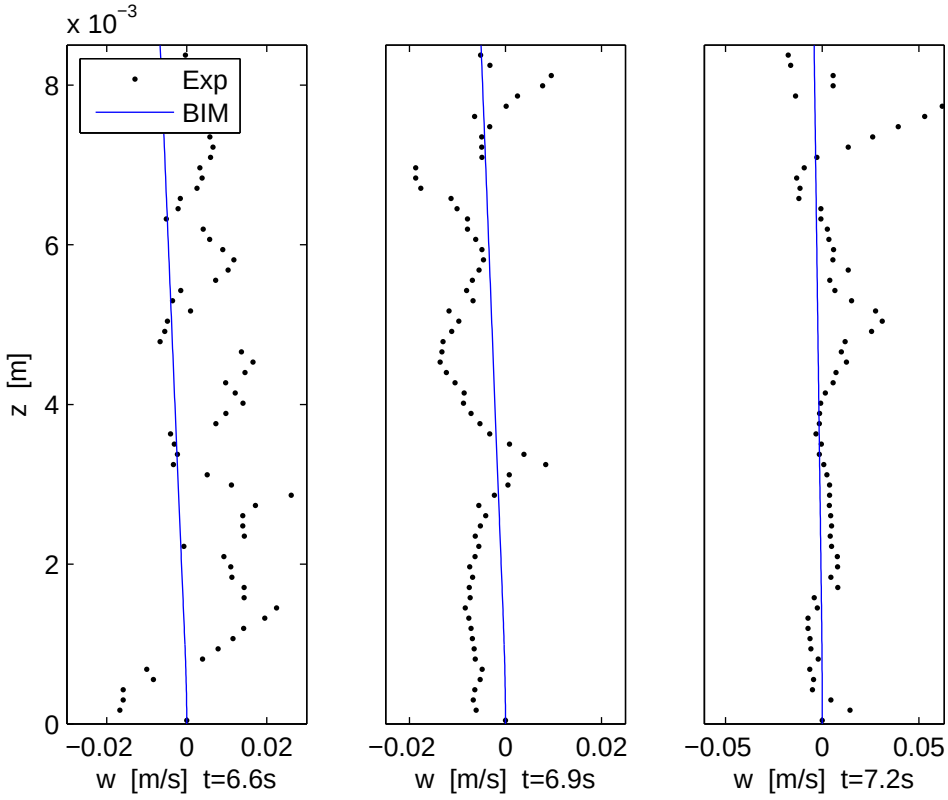

Figure 3.22: Velocity profiles of w for case 30 FOV3, at s=0.803 m

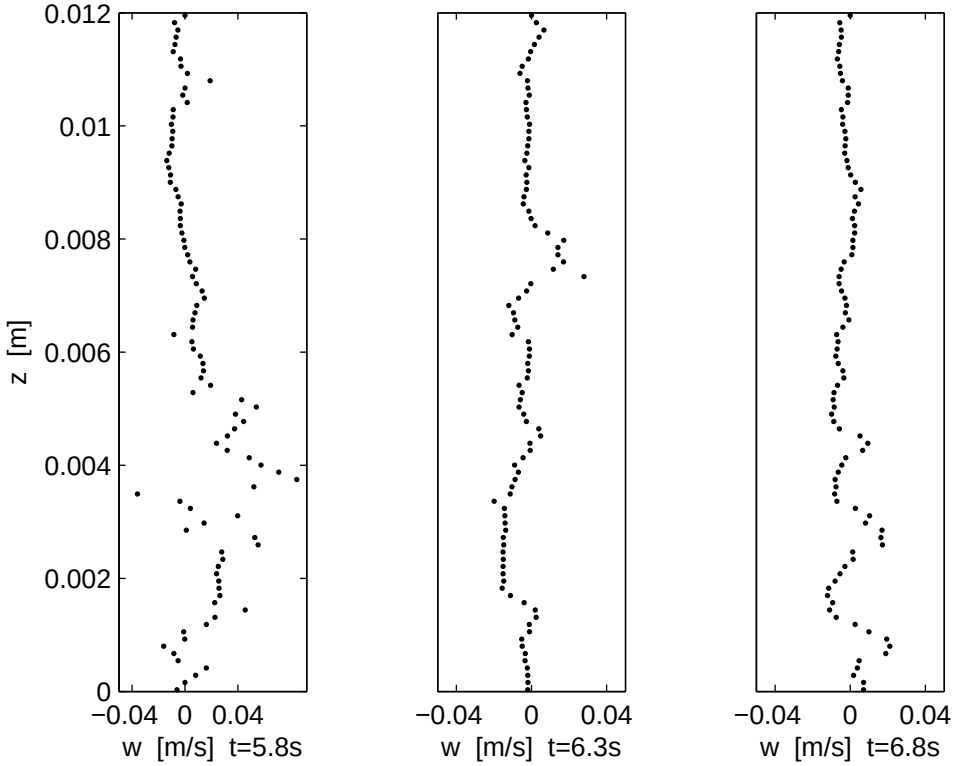

Figure 3.23: Velocity profiles of w for case 50 FOV3, at s=0.803 m

Chapter 4

Tracing of the moving shoreline

The tracing of the moving shoreline is important since it will reveal where during the inundation the experiment and theory differs, which provides useful information for the conclusion of what causes the lower maximum run-up heights in experimental results compared with theoretical results.

4.1 Experimental setup

The recording device for the tracing of the moving shoreline is a Photron APX with 1024×1024 pixels resolution and framerate of 250-1000 fps, depending of the incoming wave. The camera is mounted above the beach with the same inclination as the beach to avoid any unfavorable effects in the images that are to be processed. As lightsource a Dedolight 400D is used. The water is dyed with green color and a white PVC-film is attached on top of the beach to achieve a marked difference between the beach and the wavefront. An ultra sonic wave gauge is placed at x=-2.045 m and used to check the incoming wave and as input to the numerical model, a detailed description of the gauge is given in section 3.2. The setup is visualized in figure 4.1. The camera and the gauge is is synchronized with the wave paddle using a trigger system with t=0 as the paddle start.
To cover the whole inundation phase the camera is moved along the beach which results in several field of views for each case with 2 centimeters overlap in between them, and with a separate coordinate system for each field of view. The maximum inundation length is also checked visually and marked at the beach, as a safety check to the results from the recordings.
To make sure that the quality of the beach do not affect the inundation, a set of experiments with the PVC-film attached underneath the beach instead of on top of the beach is recorded. Due to unfavorable shadow effects the quality of the images is reduced and only the start of the inundation is recorded. The maximum inundation length is visually checked. The results agrees well with the results from the experiments with PVC-film attached on top of the beach and

the conclusion is that the PVC-film does not affect the results.

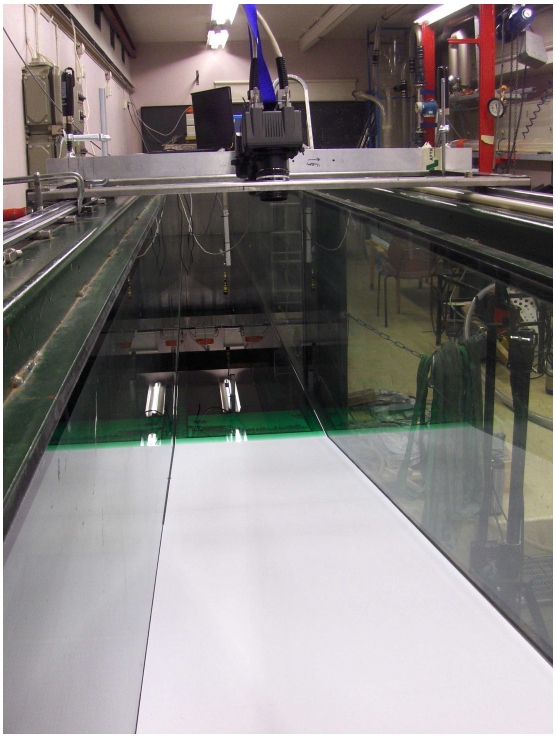

Figure 4.1: Experimental setup

4.2 Measurements and postprocessing

For the processing, a script written in matlab is used. The script uses the images as input and gives the timesteps and the median position of the shoreline as output. The main feature in the script is the function `edge`. This function takes a grayscale image as input and returns a black and white image, with white pixels where the function detects edges and black pixels elsewhere. There are several methods for this function, and the one used is `canny` which finds the edges in the input image by looking for local maximum values of the gradient of the image. The method applies two threshold values to the gradient, a high threshold for low edge sensitivity and a low threshold for high edge sensitivity. The high threshold is found with the function `graythresh`, which computes a global threshold value from the input image. The low threshold is 0.4 times the high threshold. Edges found by the weak threshold value are only included in the output image if they are connected to strong edges. In some of the images the illumination has been unfavorable and a threshold value found manually had to be used.
To avoid noise in the image, objects that are relatively small and weak (marks on the beach or particles in the water, for example) are filtered out by the function

`imopen` before the edges are detected. Noise that is not detected by `imopen` is efficiently sorted out by taking the median of the edges found, since the noise always is smaller than the actual wavefront. In figure 4.2 the input image and the detected edges are visualized.
Finally, the median pixel position of the wavefront is converted into centimeters with the function `cp2tform` and linear transformation. The transformation requires control pair points, which are found from the recorded coordinate system. The output files contains two columns, one with time and one with the median position of the wavefront.
The matlab script is presented in Appendix D.

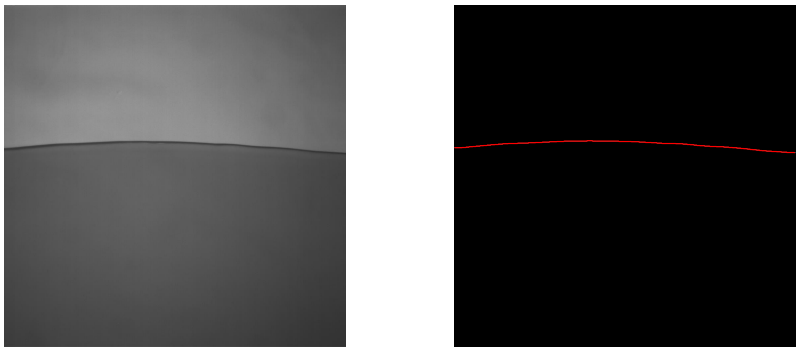

Figure 4.2: Left: Input image. Right: Detected edges

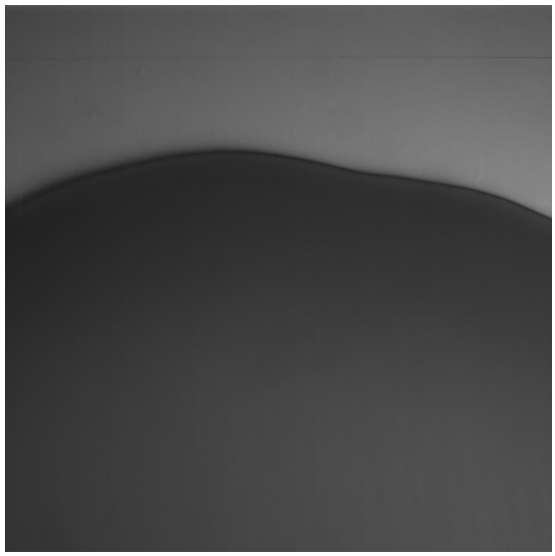

Figure 4.3: Case 50 at maximum inundation

As seen in figure 4.3, there is a transverse variation of the shoreline. This is most pronounced in the late stage of the inundation phase and is probably due

to the deformation of the beach, mentioned in section 3.2. During the rest of the inundation it is within a few millimeters and considered negligible. The largest effect of this phenomena is displayed in case 50, seen in figure 4.4 and figure 4.5, where the maximum and minimum s-positions of the shoreline are plotted with the median position at selected instances of time. In table 4.1 median, maximum and minimum values of the shoreline position at the maximum inundation for each case are presented. It should be noted that the field of view is varying from 28.5×28.5 cm, in the field of view closest to s=0, to 17.7×17.7 cm in the field of view located at the maximum inundation of case 50. Hence, only the center of the shoreline is captured since the wavetank is 0.5 m wide and the actual minimum values of the shoreline position are probably even smaller.
It should also be noted that the repeatability is good for case 10, 20 and 30 throughout the inundation. But for case 40 and 50 the results reveals that the repeatability in the later stage of the inundation is poorer, the maximum inundation for case 40 differs 6 mm between the runs and for case 50 the maximum inundation differs 26 mm between the runs.

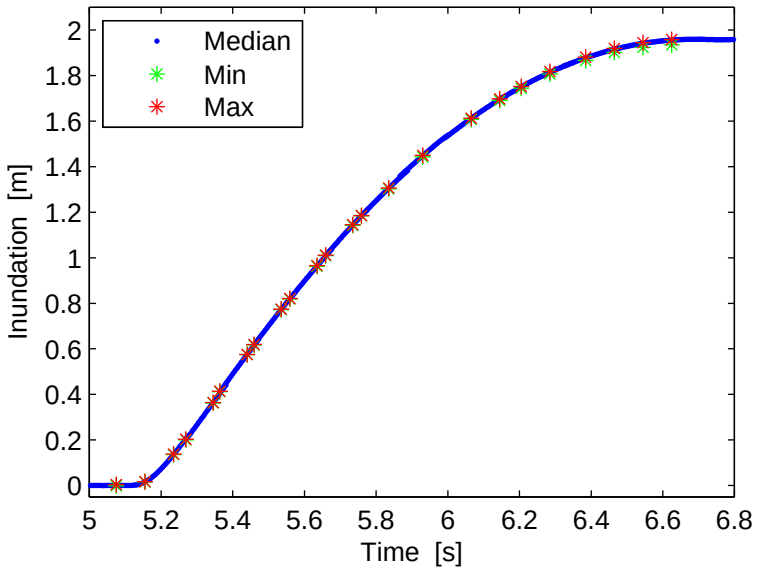

Figure 4.4: Case 50. Median, maximum and minimum position of the shoreline

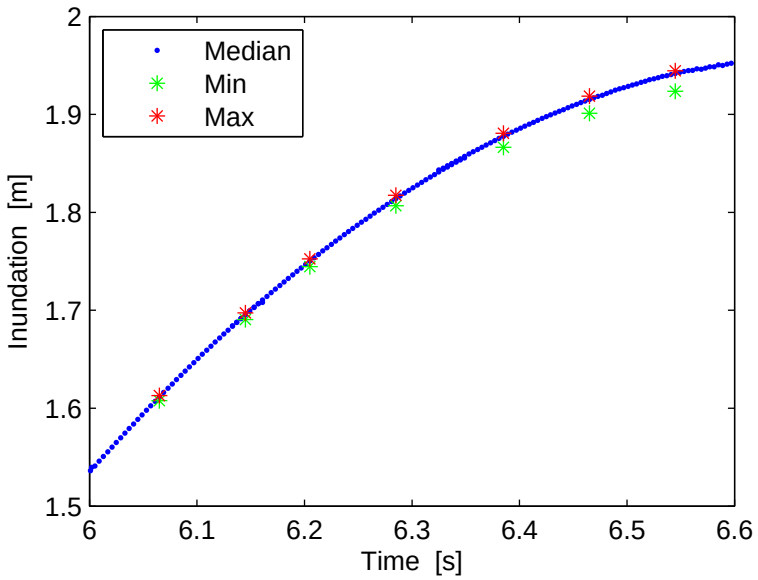

Figure 4.5: Case 50. Median, maximum and minimum position of the shoreline at the later stage of the inundation

4.3 Results

The results of the tracing from the moving shoreline is visualized in figure 4.6-4.10. As visualized in figure 4.6-4.8, the discrepancies between theory and experiment is most pronounced in the later stage of the inundation. The run-up heights are given in table 4.2, where the run-up height is given as the inundation length times $\sin\theta$, where θ is the inclination of the beach, and the deviation is calculated by the formula (|experimental-theoretical|/theoretical)$\times$100. The measured run-up heights are significantly smaller than the theoretical ones and the deviation increases with the amplitude of the incoming wave as seen in table 4.2.
The figures also reveal that the start of the inundation in the experimental results are delayed compared with theory. This effect is most pronounced in case 10, but the effect is also present in case 20 and case 30. The start of the inundation for case 10, 20 and 30 are visualized in figure 4.11-4.13. The delay in the start of the inundation is most likely due to surface tension. The surface tension is a constant property of the fluid and will affect the smaller waves with less momentum in a larger scale than it will affect the incident waves with larger amplitude. Once the wave has started the inundation, the velocities in the wave are larger than in the theoretical models, and for case 20 the wave catches up with the results from the BIM model at t=6.18 s, before it separates again at t=6.28 s. In case 30 the wave catches up with the results from the BIM model at t=5.57 and is ahead of the theory a short while before it separates at t=5.80 s.
There are two observations in this investigation that implies that the main reason to the discrepancies between the experimental results and the theory considering the maximum run-up height is the viscous effects inside the boundary layer. As presented in table 4.2 the deviation increases with increasing amplitude of the incoming wave. As mentioned in section 3.3 the run-up tongue becomes long and thin for the larger waves and the viscous effect will have a larger influence on the flow during run-up. Also, the surface tension causes a delay in the start of the inundation, but for case 20 and 30 the wave catches up with theory after a short time which implies that the delay only affects the the start of the inundation and not the maximum run-up height.

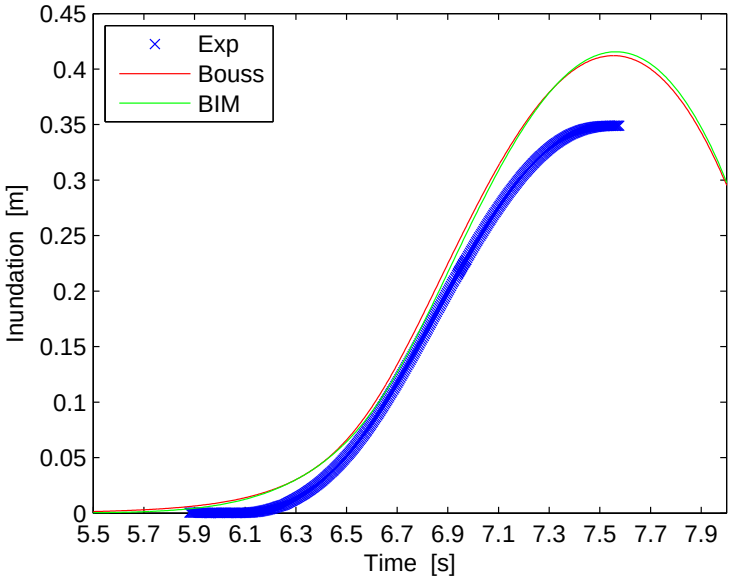

Figure 4.6: Case 10. Inundation

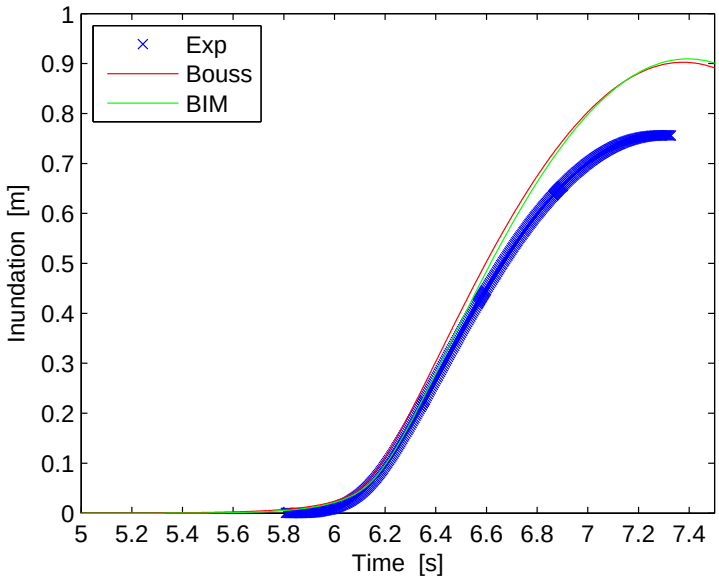

Figure 4.7: Case 20. Inundation

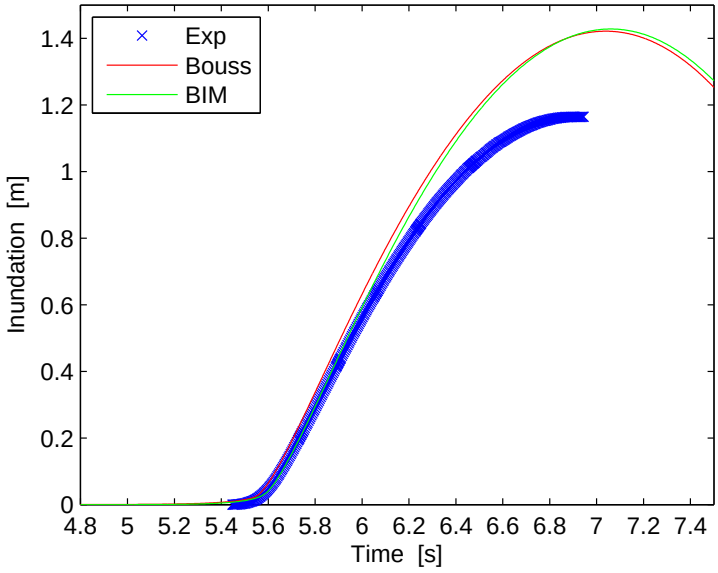

Figure 4.8: Case 30. Inundation

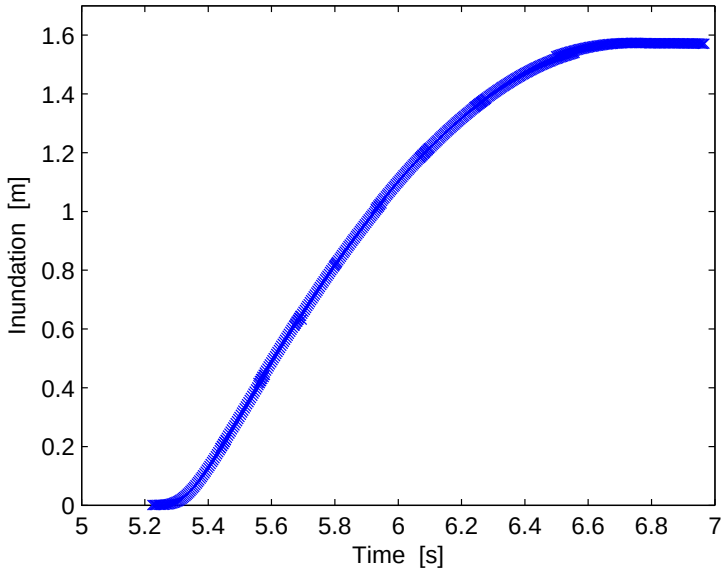

Figure 4.9: Case 40. Inundation

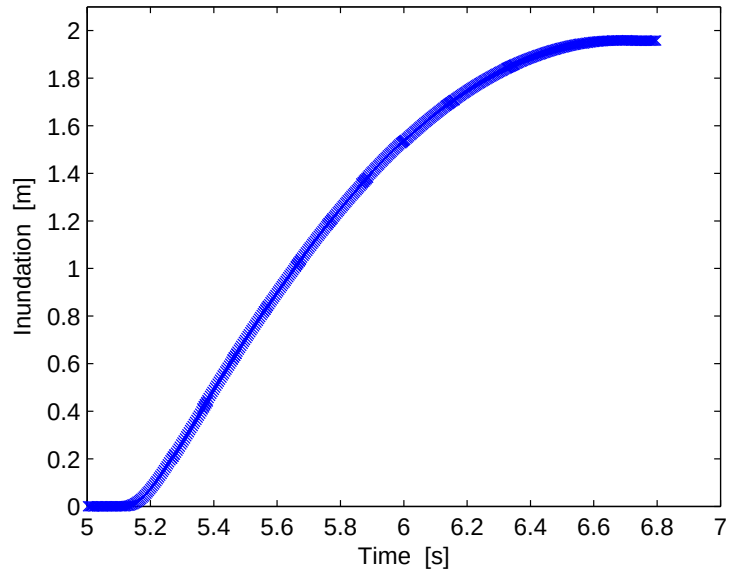

Figure 4.10: Case 50. Inundation

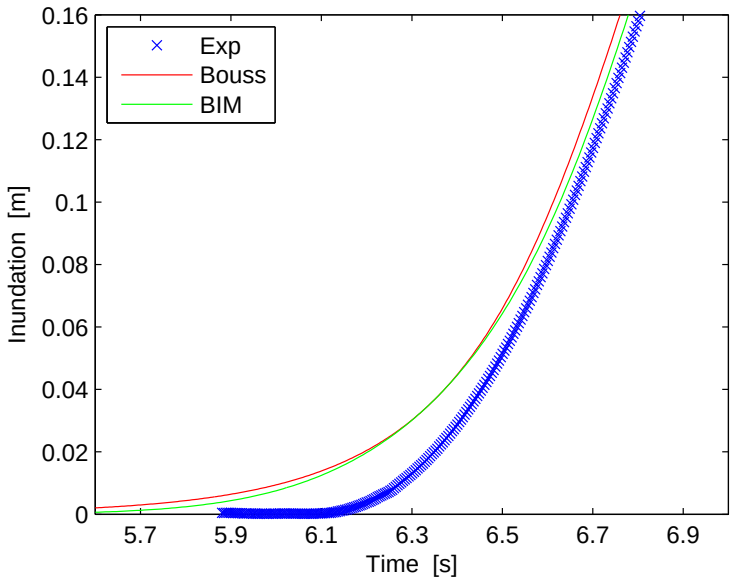

Figure 4.11: Case 30. Start of inundation

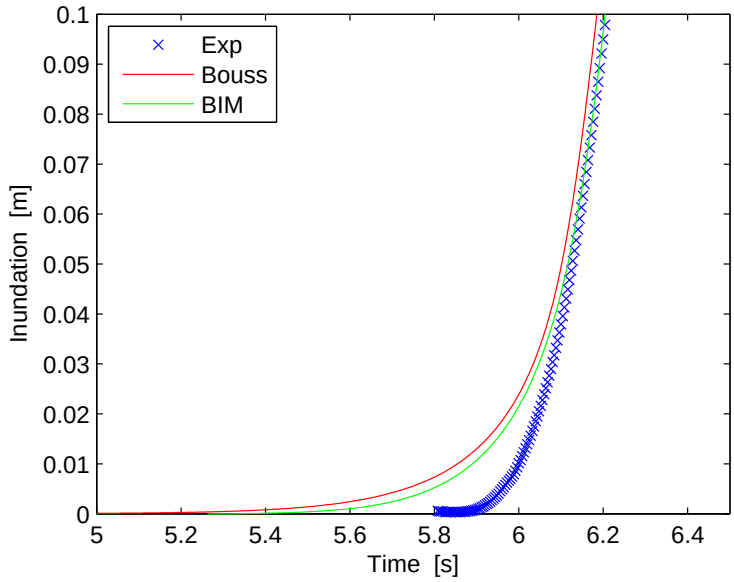

Figure 4.12: Case 20. Start of inundation

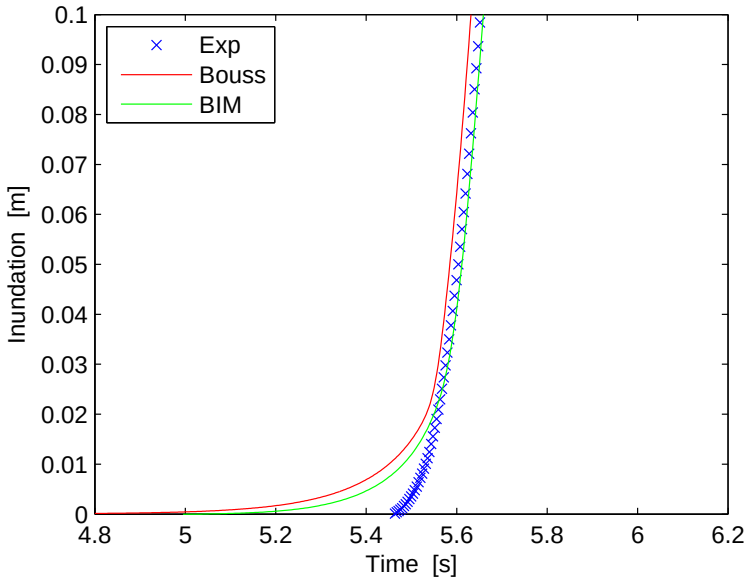

Figure 4.13: Case 30. Start of inundation

Case	A/d	**Inundation** (cm) median	max	min	**R/A** median	max	min
10	0.0977	34.9	35.1	34.6	3.10	3.12	3.07
20	0.195	75.6	75.8	75.0	3.37	3.38	3.34
30	0.292	116.4	116.7	115.6	3.46	3.47	3.44
40	0.388	157.4	157.6	155.9	3.52	3.53	3.49
50	0.481	196.8	197.1	194.7	3.55	3.56	3.51

Table 4.1: Median, maximum and minimum values of the shoreline position at the maximum inundation

Case	A/d	**R/A** Exp	Bouss	BIM	Deviation Bouss (%)	Deviation BIM (%)
10	0.0977	3.12	3.66	3.69	14.8	15.5
20	0.195	3.38	4.02	4.05	15.9	16.5
30	0.292	3.47	4.22	4.24	17.8	18.2
40	0.388	3.53	-	-	-	-
50	0.481	3.55	-	-	-	-

Table 4.2: Maximum run-up heights, experimental and numerical models

4.3.1 Start of inundation

To be able to collect more information about the delay in the start of the inundation, a new set of experiments are performed. A high speed camera is placed outside the wavetank, with a small angle towards the shoreline to exclude unfavorable effects from the full adhesion at the wall. As lightsource a Dedolight 400D is used which is placed outside the tank at the deep water region and directed towards the shoreline. When the wavefront gains height before the start of the inundation, a shadow from the wave is thrown at the beach and the shadow is used as a measurement of the height of the wavefront. Figure 4.14 shows the wavefront of case 10 0.05 seconds before the wave starts to climb the beach. To obtain a relation between the length of the shadow and the height of the wave a small block is placed in the focal area and the shadow from the block is measured. This provides a linear relation between the waveheight and the length of the shadow. The images are manually processed by measuring the length of the shadow in pixels and then converting the pixels to meter.
In addition to the camera, two gauges are placed at positions x=-0.01165 m and x=0 m, hereafter referred to as gauge 2 and gauge 3, set to sample at 200 Hz. Gauge 2 serves the purpose to check the wave before it starts to climb the beach, and the results have revealed good agreement with theory. As observed in section 3.3, the BIM model is the model that performs best. Gauge 3 serves as a quality check for the results from the images. The data from gauge 3 are influenced by the angle of the beach, which causes an uncertainty in the results.
The results from the images are plotted in figure 4.15 revealing that the wave is gaining height before it starts to climb the beach. These results confirm the assumption that it is the surface tension that causes the delay of the inundation, since the height of the wavefront decreases with increasing amplitude of the incident wave. Results from gauge 3 is given in table 4.3 together with the results from the images for comparison. The results from gauge 3 differs slightly from the results from the images, and this is most likely caused by the uncertainty of the gauge due to the angle at the target (see section 3.2).

Case	A/d	Time [s]	Images [mm]	Gauge 3 [mm]
10	0.0977	6.10	3.2	3.1
20	0.195	5.89	2.9	3.2
30	0.292	5.44	2.4	2.7

Table 4.3: Measured height of the wavefront at the time instant the wave start to climb the beach

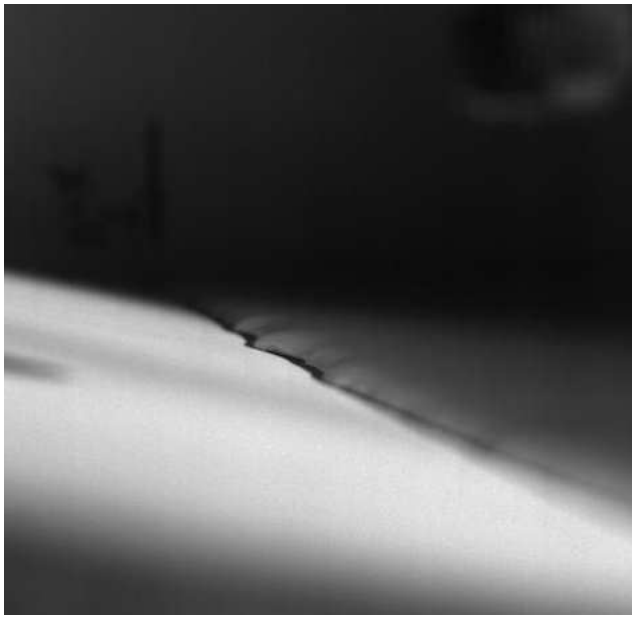

Figure 4.14: Case 10 t=6.05s, 0.05 seconds before the wave starts to climb the beach

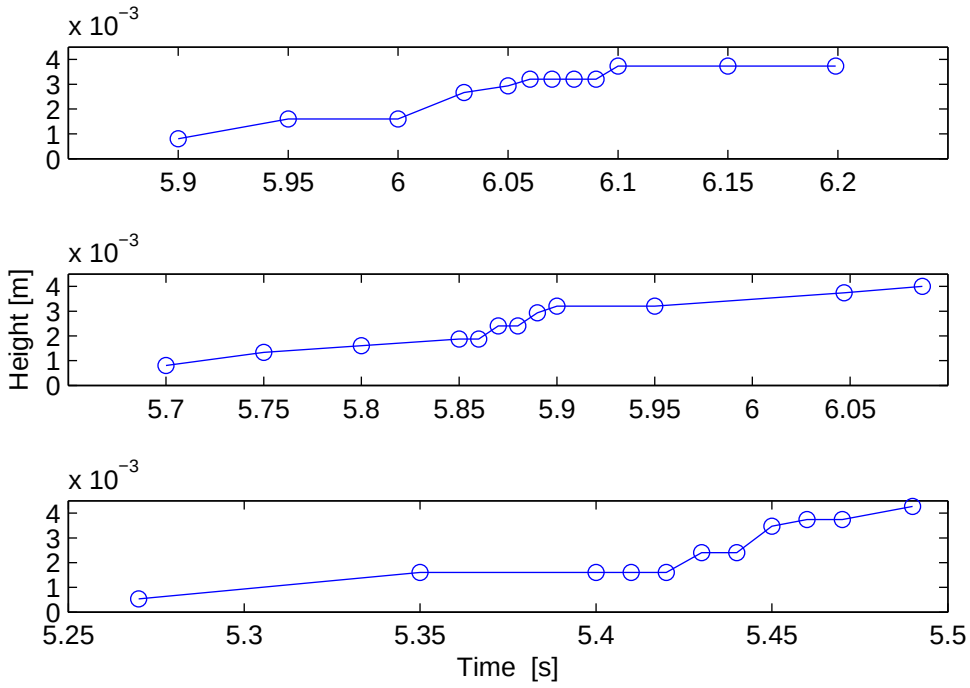

Figure 4.15: Measured height of the wavefront. Upper: case10, middle: case20, lower: case30

4.3.2 Surface tension

Since the delay of the start of the inundation is caused by the surface tension, an investigation of the surface tension is performed by Dr. D. Laskovski. The surface tension is measured in both the colored water that is used in the experiments and pure water and found to be 71.7mN/m in both cases. The contact angle between the water and the beach is measured, given in table 4.4 The conclusion made by Dr. Laskovski is that both liquids wet the PVC far greater than the PETG substrate and that the colored water is forming some form of repulsion with the white film compared to the water. This may be related to the porosity of the white film with respect to the dye or the surface energies. These results suggest that the best scenario for large run-up would be pure water on PVC.

No further work is done in the investigation of the surface tension and contact angle.

Beach	**Contact angle**	
	colored water	pure water
PETG	73°	73°
PVC	65°	61°

Table 4.4: Contact angles

Chapter 5

Conclusion

5.1 Discussion and conclusion

In this thesis, run-up of solitary waves have been investigated. The focus has been to investigate the reasons for the deviation between theory and experiments considering the maximum run-up height. To provide insight in possible reasons for the deviation, the surface elevation at the beach, the velocity fields close to the beach and tracing of the moving shoreline during the inundation have been investigated.
Due to the viscosity in the fluid there exists a thin boundary layer in the region close to the beach. To be able to include the boundary layer in the numerical models, the flow is divided into an outer inviscid region and an inner viscous region. Two separate models are used to describe the outer flow, the Boundary integral model (BIM) which is based on full potential theory and the Boussinesq-model which is based on dispersive non-linear long wave theory. It is revealed that the BIM-model is the one that performs best. In this chapter, the discussion is based on the BIM-model as the model, for comparison with theory for the outer flow and as boundary condition for the boundary layer computations.

In the investigation of the surface elevation, it is found that the agreement between experiments and theory is excellent at the deep water region. The experimental results agree well with theory in early in the inundation phase. At the later stage of the inundation there are some discrepancies between theory and experiments.

The investigation of the velocity fields reveals that there are well defined boundary layers in all the cases in FOV2, located near the still water/beach intersection. The boundary layer will cause a reduced onshore volume flux during the inundation in comparison to theory for an inviscid flow, which will cause lower run-up height. The boundary layer stays laminar and well defined in FOV2 through-

out the run-up and run-down. It is found that flow reversal starts earlier in the boundary layer than in the outer flow. A consequence of the reversal in the boundary layer is that the z-component of the velocity will increase in negative z-direction and there will arise a draining effect in the wave, which further reduces the run-up height. In comparison to theory, discrepancies in the velocities in the outer flow is revealed. The velocities in the outer region are larger than the ones predicted by theory. One explanation might be the delay at the start of the inundation caused by the surface tension which in turn causes larger velocities in the wave early in the inundation. If this was the cause, the discrepancies would be more pronounced in case 10 than in case 20 and 30 but this is not the case and the discrepancies remains unexplained.
There are instabilities in the flow during the run-up. For case 50, there are instabilities in FOV1, located in the middle of the tank at the lower end of the beach. These instabilities is not observed in FOV2. A suggestion is that case 50 is very labile, and that the deflection of the beach during inundation causes these instabilities. In case 10, 20, 30 and 40 the boundary layer appears to stay laminar and stable in both FOV1 and FOV2.
Further up the beach, in FOV3, case 30, 40 and 50 reveals flow instabilities while case 10 and 20 do not reach the camera. Visual observation of the recorded images reveals that the flow is laminar in the tip of the wave, and that after a short while instabilities are generated in the boundary layer, spreading out to the outer flow. These instabilities might appear to be a display of transition to turbulence. It is reasonable to assume that the turbulent energy dissipates during run-down and the boundary layer stabilizes again before it reaches the lower end of the beach.
The observed instabilities will most likely affect the run-up height but the manner in which it will is not determined.

The tracing of the moving shoreline reveals that the discrepancies between theory and experiments is most pronounced in the later stage of the inundation, but that there also are discrepancies in the start of the inundation caused by the surface tension. The start of the inundation is further investigated and it is found that the wavefront gains height before it starts to climb the beach. This causes a delay in time in the experimental results compared to theory which is most pronounced in case 10. Once the wave starts to climb the beach, the shoreline velocity is larger than the velocity predicted by the numerical models, and in case 20 and case 30 the wave catches up with theory after a short while before it separates from it again. It is not likely that the delay caused by the surface tension affects the maximum run-up height, but it does affect the velocity in the flow at the early stage of the inundation. The deviation between theory and experiments in the later stage of the inundation is most likely due to the viscous effects in the boundary layer. The viscosity affects the waves with higher amplitude more than it does the waves with smaller amplitude since the higher amplitudes causes

a long and thin run-up tongue. The results reveal that the deviation between experiment and theory, with respect to the R/A ratio, increase with increasing amplitude of the incident wave.

Based on the results from the experiments, one might assume that the inviscid models' over-prediction of the maximum run-up height mainly is caused by the viscous effects in the boundary layer. The surface tension affects the inundation in the early stage, but it is not likely that it affects the maximum run-up height.

5.2 Suggestions for further work

To be able to further investigate the boundary layer, for instance to do calculations of the dissipation and drag, the quality of the vectors need to be improved. The seeding in the PIV measurements where not optimal and should be improved, either by using smaller particles or by applying PTV instead of PIV. During the postprocessing, between 75% and 95% of the vectors where good quality and the results are considered reliable for the purpose of detecting and visulizing the boundary layers. It would be of great interest to determine where the instabilites in the boundary layer appear during inundation, and also investigate if these instabilities appear in case 10 and case 20 as well. The observed instabilites seem to be the apperance of turbulence, and it would be interesting to find the mean velocity in the flow and determine the fluctuations in the velocity field. It would also be interesting to investigate how the instabilites affect the maximum run-up height. Observing the outer velocity in the flow at the start of the inundation, discrepancies between theory and experiment are displayed. This is unexpected and should be further investigated.

Appendix A

A note on a BIM model made for runup

This chapter is copied from the intranet at the University of Oslo and is written by Geir K. Pedersen

Introduction

This note is a brief description of a full potential flow model with particular adaptations to moving shorelines. The model is closely related to the higher order technique of [19, 20], while the formulation differs from the standard references [21, 22, 23]. However, while these references employ high order polynomials for interpolation along the contour we use cubic splines. This makes inclusion of boundary conditions simpler and does allow for the inclusion of a moving shoreline in particular.

At the shoreline point we assume analyticity which in principle excludes cases with contact angles larger than 90°. Also some other features, such as the numerical integration procedure along the contours, differ from the references. Boundary integral methods are not efficient for the computation of very thin swash tongues that evolve during runup/withdrawal of higher waves. This is ironical since the flow may be so simple that even the shallow water equations are unnecessarily complicated (see [5]). The proximity of the surface and the bottom parts of the contour requires a smaller time step relative to the grid spacing and a higher order numerical integration than in deeper water. A runup value should then only be accepted if a systematic refinement sequence of at least three grids, with the the same integration rule, produce consistent results and point to at least three correct digits.

A.1 A boundary integral method

In the fluid the motion is governed by the Laplace equation

$$\nabla^2\phi = 0 \quad \text{for} \quad -h < z < \eta.$$

At the free surface ($z = \eta$) the Bernoulli equation is expressed as

$$\frac{\mathrm{D}\phi}{\mathrm{D}t} - \frac{1}{2}(\nabla\phi)^2 + \eta = 0 \tag{A.1}$$

The kinematic condition at the surface is written in the Lagrangian form

$$\frac{\mathrm{D}\eta}{\mathrm{D}t} = \frac{\partial\phi}{\partial z} \quad \frac{\mathrm{D}\xi}{\mathrm{D}t} = \frac{\partial\phi}{\partial x},$$

where (η, ξ) is the position of a surface particle. At rigid boundaries (bottom or sidewalls) we have

$$\frac{\partial\phi}{\partial n} = 0,$$

where n denotes the direction normal to the boundary.
This model is related to the high order technique of [20]. However, to allow more flexible boundary conditions, as sloping beaches, the high order polynomials are replaced by cubic splines for the spatial interpolation between nodes. Accordingly the order of the temporal scheme is reduced to third order accuracy. The key features then become

- Lagrangian particles are used along the free surface. At other boundaries both fixed and moving nodes may be employed
- Cauchy's formula for complex velocity ($q = u - iv$) is used to produce an implicit relation between the velocity components along the surface

$$\alpha i q(z_p) = \mathrm{PV} \oint_C \frac{q(z)}{z_p - z} dz \tag{A.2}$$

  where α is the interior angle. Following [20] the integral equation (A.2) is rephrased in terms of the velocity components tangential and normal to the contour, denoted by $u^{(s)}$ and $v^{(s)}$, respectively. Invoking the relation

$$u^{(s)} - iv^{(s)} = \mathrm{e}^{i\theta}(u - iv),$$

  where θ is the angle between the tangent and the x-axis, we then obtain

$$\alpha i(u_p^{(s)} - v_p^{(s)}) = \mathrm{e}^{i\theta_p}\mathrm{PV} \oint_C \frac{u^{(s)} - iv^{(s)}}{z_p - z} ds. \tag{A.3}$$

For rigid boundaries, where the normal velocity is known, the real component of this equation is imposed, while the imaginary component is used at free surfaces, where u_s is known from the integration of the Bernoulli equation. The equation set is established by collocation in the sense that z_p runs through all nodes to produce as many equations as unknowns (see figure A.1).

- Cubic splines for field variables – solution is twice continuously differentiable
- Combination of Taylor series expansion and multi-step technique used for time integration. This allows for variable time stepping. For instance, ϕ_p is advanced one time step n to $n+1$ according to

$$\phi_{(n+1)} = \phi_{(n)} + \Delta t_{(n)} \left(\frac{\mathrm{D}\phi}{\mathrm{D}t}\right)_{(n)} + \frac{1}{2}\Delta t_{(n)}^2 \left(\frac{\mathrm{D}^2\phi}{\mathrm{D}t^2}\right)_{(n)} + \frac{1}{6}\frac{\Delta t_{(n)}^3}{\Delta t_{(n-1)}} \left(\frac{\mathrm{D}^2\phi}{\mathrm{D}t^2}_{(n)} - \frac{\mathrm{D}^2\phi}{\mathrm{D}t^2}_{(n-1)}\right).$$

  The last, backward difference both increases the accuracy and stabilize the scheme. The first temporal derivative of ϕ is obtained from the Bernoulli equation. We then also obtain the local derivative, $\frac{\partial\phi}{\partial t}$, that is used to define a boundary value problem for the temporal derivatives of the velocity. This is identical to the problem for the velocities themselves, given by (A.2) or (A.3) with u and v replaced by their local time derivatives. Formulas like the one above are applied to the other principal unknowns ξ and η.
- Special treatment of corner points; invocation of analyticity.
- Like most models of this kind some filtering is required in the nonlinear case to avoid growth of noise. A five point smoothing formula is applied to this end.

In sum we have a "moderately high order" method that is lower order compared to the method [20], but at the same time less restricted at the boundaries.
The computational cycle consists of the following main steps

1. We know velocities (and more) at t. Time stepping by discrete surface condition give ϕ (potential) and particle positions at the surface for $t + \Delta t$
2. ϕ at surface yields the tangential velocity at the surface
3. Crucial step: Tangential velocity at surface and bottom condition (normal velocities) yield equations for the other velocity component through the integral equation (A.3) that is equivalent to the Laplace equation
4. $\partial\phi/\partial t$ is obtained from the Bernoulli equation (A.1). The tangential component of the temporal derivative of the velocity is then obtained, in analogy to step 2, and the linear equation set from step 3 is solved with a new right hand side to obtain the remaining component of $\partial\mathbf{v}/\partial t$.

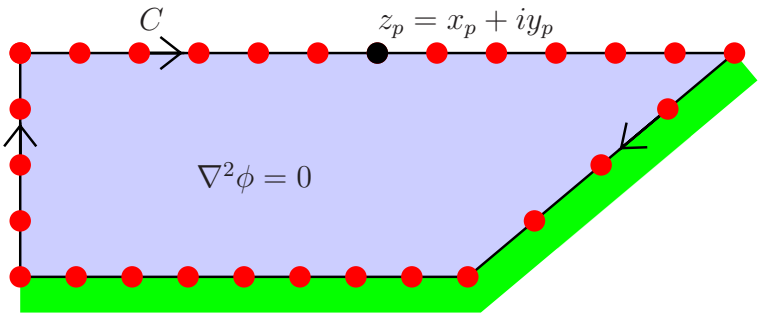

Figure A.1: Definition sketch of computational domain in BIM method

5. The Bernoulli equation is differentiated, materially, with respect to t and $\frac{\mathrm{D}^2\phi}{\mathrm{D}t^2}$ is computed.

6. Now the first and second order Lagrangian derivatives of ϕ, ξ and η are computed at $t + \Delta t$ and the cycle may repeat itself.

The whole problem is then posed in terms of the position of the fluid boundary and the velocity potential there. Values of velocities within the fluid may be obtained by choosing z_p as an interior point and put $\alpha = 2\pi$ in the Cauchy relation (A.2), which then provide explicit expressions for u_p and v_p. In the linear case the procedure is substantially simplified since the geometry is constant and matrices involved in the third step may be computed and factorized only once.

Appendix B

A note on a nonlinear boundary layer model

This chapter is copied from the intranet at the University of Oslo and is written by Geir K. Pedersen

B.1 Introduction

This is a description of method for laminar boundary layer computations. It is assumed that the outer velocity U is extracted from potential flow model or measurements. This is then used as boundary conditions for the boundary layer equations which are discretized by the Crank-Nicholson method for the linear part and a combination of upstream differences and backward time stepping for the nonlinear terms. The grid is generally non-uniform, with finer resolution close to the no-slip boundary, and the technique is validated through comparison with analytic solutions and grid-refinement studies.

B.2 Boundary layer equations on a beach

We introduce a $(s, z)-$coordinate system with the $s-$axis defined positive upwards along the beach and the $z-$axis orthogonal to the beach. We put $s = 0$ at the equilibrium shoreline on the beach. The s- and z-components of the flow outside the boundary layer $U(s, z, t)$ and $W(s, z, t)$, respectively, are supposed known, either from observations or numerical simulations. According to [6], as well as potential flow simulations, the z variation of U is very weak in the swash flow. The flow in a viscous boundary layer, (u, w), is then governed by the following momentum equation

$$\frac{\partial u}{\partial t} + u\frac{\partial u}{\partial s} + w\frac{\partial u}{\partial z} = \left[\frac{\partial U}{\partial t} + U\frac{\partial U}{\partial s}\right]_{z=0} + \nu\frac{\partial^2 u}{\partial z^2}, \tag{B.1}$$

where the terms within the bracket correspond to the gravity component along the shore and pressure gradient which is assumed equal to that of the outer flow. The continuity equation is

$$\frac{\partial u}{\partial s} + \frac{\partial w}{\partial z} = 0 \tag{B.2}$$

The no-slip boundary conditions is

$$u(s, 0, t) = w(s, 0, t) = 0 \tag{B.3}$$

and the following matching condition must also be fulfilled

$$[u(s, z, t)]_{z>>\delta_{bl}} = U(s, 0, t) \tag{B.4}$$

where δ_{bl} is the boundary layer thickness. For the linearized version the boundary value problem given by equations (B.1) through (B.4) closed form solutions may be obtained when the outer flows specified as polynomials of time.

B.3 Numerical computation of boundary layers

B.3.1 Application of the boundary value model to runup

Outer flow fields are extracted from the inviscid models. The Lagrangian solutions are interpolated onto an equidistant, Eulerian grid along the beach, which extends the whole swash zone, including an extra section on the wet side of off-shore side of the equilibrium shoreline position. An example of the resolution: for solitary waves of amplitude $0.1d$ to $0.3d$ (d is depth of wave tank) incident on 10° beach typically from $M = 50$ to $M = 400$ points have been applied on the beach yielding increments, Δs, in the range $0.22\,\text{cm} \leq \Delta s \leq 1.52\,\text{cm}$. The temporal resolution equals that of the inviscid simulation with time increments down to $\Delta t \approx 0.0004\,\text{sec}$. At a given time only a subset of the Eulerian grid is within the swash zone. During runup new grid points must be included, while points are removed during withdrawal.

In the principle the velocity of the outer flow should have been evaluated at the bottom $z = 0$. However, even though this value may be extracted from the Boussinesq solution [5] we instead use the depth averaged value. The difference is in general very small. The forcing term (within brackets on right hand side) of the momentum equation (B.1) then becomes $F(s, t) \equiv \frac{\partial U}{\partial t} + U\frac{\partial U}{\partial s}$, where U is the depth averaged velocity from the Boussinesq model, or the bottom velocity from the BIM model.

B.3.2 Scaling

As the boundary layer method is formulated and implemented in software it may accept input in any consistent scaling, for instance SI units. However, it is

convenient to work with dimensionless variables with the depth d as length scale and the shallow water wave celerity $\sqrt{gd}$ as velocity scale. This is the scaling which is used in the Boussinesq and BIM models. The momentum boundary layer equation then reads

$$\frac{\partial u}{\partial t} + u\frac{\partial u}{\partial s} + w\frac{\partial u}{\partial z} = \left[\frac{\partial U}{\partial t} + U\frac{\partial U}{\partial s}\right]_{z=0} + \frac{1}{Re}\frac{\partial^2 u}{\partial z^2}, \tag{B.5}$$

where $Re = \frac{d\sqrt{gd}}{\nu}$ is a kind of wave-tank Reynolds number. It should be noted that this is not comparable to the standard Reynolds numbers used for stating stability limits for Blasius profiles. In short, the dimensionless kinematic viscosity coefficient is $1/Re$.

B.3.3 The discretization

A z interval $[0, B]$ is discretized by the grid $\{z_i\}$ such that z_i are given in increasing order with $z_0 = 0$ and $z_N = B$. Generally B corresponds to 2 cm. In the s, z plane we thus have a $M \times N$. Generally the grid is non-uniform in the z direction to allow for a finer resolution close to the boundary $z = 0$. We identify the local grid increments

$$\Delta z_{i+\frac{1}{2}} = z_{i+1} - z_i, \quad \Delta z_i = \frac{1}{2}(z_{i+1} - z_{i-1}).$$

Defining $w_{k,i}^{(n)} \approx w(s_0 + (k-1)\Delta s, z_i, n\Delta t)$, where Δt is the time increment, we discretize the heat equation (B.1), using the Cranck-Nicholsen method for the linear parts and upwind/backward representation for the nonlinear parts

$$\frac{u_{k,i}^{(n+1)} - u_{k,i}^{(n)}}{\Delta t} + u_{k,i}^{(n+1)}[\frac{\partial u}{\partial x}]_{k,i}^{(n)} + w_{k,i}^{(n)}\frac{u_{k,i+1}^{(n+1)} - u_{k,i+1}^{(n+1)}}{2\Delta z_i} = \frac{Q_{k,i+\frac{1}{2}}^{(n+\frac{1}{2})} - Q_{k,i-\frac{1}{2}}^{(n+\frac{1}{2})}}{\Delta z_i} + F_k^{(n+\frac{1}{2})}, \tag{B.6}$$

where

$$Q_{k,i+\frac{1}{2}}^{(n+\frac{1}{2})} = \nu\left(\frac{u_{k,i+1}^{(n+1)} + u_{k,i+1}^{(n)} - u_{k,i}^{(n+1)} - u_{k,i}^{(n)}}{2\Delta z_{i+\frac{1}{2}}}\right),$$

and $[\frac{\partial u}{\partial x}]$ denotes the upwind difference. If an upwind difference involves a value that is not defined, a downwind difference is used instead. The pressure term, F, is consistent with the nonlinear terms on the left hand side of (B.6). As a consequence the outer flow can be exactly reproduced by the discrete momentum equation. The boundary conditions become

$$u_{k,0}^{(n+1)} = 0, \quad u_{k,N}^{(n+1)} = U_k^{(n+1)}, \tag{B.7}$$

while w is obtained from the continuity equation according to

$$w_{k,i}^{(n+1)} = \sum_{j=0}^{i-1} \Delta z_{j+\frac{1}{2}} \frac{u_{k+1,j}^{(n+1)} + u_{k+1,j+1}^{(n+1)} - u_{k-1,j}^{(n+1)} - u_{k-1,j+1}^{(n+1)}}{2\Delta s} \tag{B.8}$$

If k is adjacent to a non-defined s-node (either dry or outside the grid on the seaward side) one sided derivatives are used for u in this expression. When all quantities at time n is known, (B.6) and (B.7) yield a set of M, or less, independent tridiagonal equations for the nodal values for u at time $n+1$.
When the shoreline surpasses a new grid point, say m, the row $k = m$ is included in the computation and initial conditions set to $u_{m,i}^{(n)} = U_m^{(n)}$.
The linear version of (B.6), corresponding to the Crank-Nicholson method, is of second order accuracy and is unconditionally stable. When ν and w are set to zero the discretization corresponds to a second order integration along characteristics. For the combined equation we may no longer claim second order accuracy, but no instability has been encountered. The critical parameter for the accuracy is Δs and the main source of error is linked to the moving shoreline. This is discussed in somewhat more detail below.

B.3.4 Grid generation

Non-uniform grids, with smoothly varying distribution of nodes, are readily constructed by means of a mapping from a an enumeration coordinate, ζ, to z

$$z = z(\zeta), \quad z(0) = 0, \quad z(N) = B,$$

An approximate local grid increment is then $\Delta z(\zeta) = \frac{\mathrm{d}z}{\mathrm{d}\zeta}$ We desire a finer grid at $z = 0$ than at $z = B$ and define stretch factor, S, as the ratio between the corresponding increments

$$S = \frac{\frac{\mathrm{d}z(n)}{\mathrm{d}\zeta}}{\frac{\mathrm{d}z(0)}{\mathrm{d}\zeta}}.$$

Several distribution functions, f, have been tested, without significant differences in the performance. Two simple nonuniform grids are found as

Quadratic	$z = a\zeta + \frac{1}{2}b\zeta^2$	$a = \frac{2B}{(S+1)N}$	$b = \frac{a(S-1)}{N}$
Exponential	$z = \frac{a}{b}\left(e^{b\zeta} - 1\right)$	$a = \frac{bB}{S-1}$	$b = \frac{\ln S}{N}$

We have mainly employed with $S = 4$.

B.3.5 Performance

The computations of the boundary layer flow depends on the accuracy of the inviscid simulation in the first place, on the resolution of the extracted outer

flow field (Δs) and the vertical resolution in the boundary layer model (N and S). Concerning the modelling of the boundary layer itself there are three main problems that are all linked to the shoreline

1. At the shoreline he physical model of a viscous layer and an outer inviscid flow is not correct. First, in our model the thickness of the boundary layer at a position s grows in proportion to $\sqrt{t - t_0(s)}$, where t_0 is the time when the shoreline reaches s. In the swash zone the inviscid flow depth will grow in proportion to $t - t_0(s)$. Hence, for small $t - t_0$ the boundary layer will be thicker than the flow depth. Secondly, and more fundamentally, the vicinity of the moving shoreline is governed by some kind of contact point dynamics, where the fluid particle at the shoreline is stuck to the beach, while new fluid presumably is rolled onto the beach during runup. We have not been able to measure any details in the dynamics of the fluid tip and it is beyond modeling at present. Still, only a short distance from the shoreline we do observe a regime with laminar boundary layer motion in the experiments.

2. Also in the linear approximation the initial evolution of the boundary layer is abrupt and thus difficult to reproduce accurately by a numerical technique. However, with the resolutions employed the accuracy in the linear solutions are very good even for quite small times. The next point is more crucial.

3. New grid rows are included in the boundary layer computations in a stepwise manner according to the shoreline motion. At the instant a new row is introduced the velocity is initialized from the outer flow. Consequently there will be a strong along-shore velocity gradient in the boundary layer with a correspondingly large vertical velocity component. This is a plausible mechanism from a physical point of view and it leads to a much faster growth of the boundary layer in the non-linear than in the linear description. However, the mechanism is hard to catch accurately in the numerical model.

In line with the last point the nonlinear solutions are hardest to obtain accurately and the critical parameter is Δs. Therefore we will show some details on the evolution of the boundary value profiles for the most nonlinear case $A/d = 0.295$ in figure B.3.5. At first glance the profiles may look very similar for all times. However, a closer scrutiny reveals a marked deviation for the earliest time displayed, corresponding to a slower boundary layer growth for the coarser resolutions. Later the deviations are diminished. Overall, this indicates that the smallest Δs is adequate.

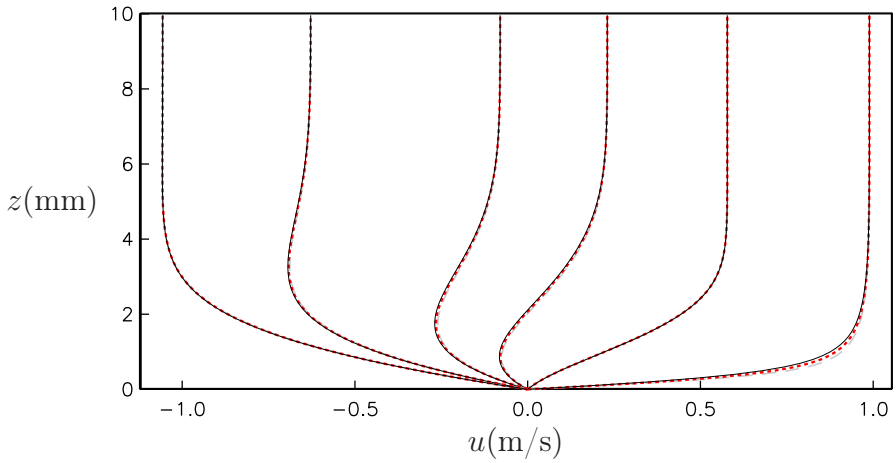

Figure B.1: Velocity profiles for $A/d = 0.295$ at $x = 1.05\,\mathrm{m}$. Long dashes, short dashes and solid lines correspond to $\Delta s = 1.52\,\mathrm{cm}$, $\Delta s = 0.76\,\mathrm{cm}$ and $\Delta s = 0.38\,\mathrm{cm}$, respectively. The times are (in seconds) 6.35, 6.55, 6.75, 6.95, 7.35 and 7.70. Since the outer flow is retarded for the range of times displayed, the graphs are ordered from right to left with increasing t.

B.4 Linear test problems

In this section we neglect the nonlinear terms in (B.1). The boundary layer equations then become the standard heat equation with a source term F:

$$\frac{\partial w}{\partial t} = \nu \frac{\partial^2 w}{\partial z^2} + F(z,t), \tag{B.9}$$

where the unknown have been renamed to w. We observe that s does not enter the equation, but may appear only as a parameter.

B.4.1 Separation of discrete equation

For $F = 0$ the heat equation (B.9) inherits the simple damped harmonic solutions

$$w = e^{\alpha t} e^{ikz}, \quad \alpha = \nu k^2.$$

For uniform resolution the corresponding solutions for the discrete problem, (B.6), read

$$w_j^{[n]} = e^{\alpha n \Delta t} e^{ikj\Delta z}, \quad \frac{2}{\Delta t} \tan\left(\frac{\alpha \Delta t}{2}\right) = \nu \frac{4}{\Delta z^2} \sin^2\left(\frac{k\Delta z}{2}\right).$$

This relation always yields a non-negative value for α which implies unconditional stability. Assuming small $\alpha\Delta t$ and $k\Delta z$ we obtain the damping relation

$$\alpha = \nu k^2 \left(1 - \frac{\Delta z^2}{12} k^2 - \frac{\Delta t^2}{12} \nu^2 k^4 + O((k\Delta z)^4, (\alpha \Delta t)^4)\right). \tag{B.10}$$

Thee is no cancellation of spatial and temporal errors. However, comparable errors due to time and space dicretization occurs when

$$\Delta z^2 \sim \nu^2 k^2 \Delta t^2.$$

Assuming the boundary layer thickness, D, to be of order $1/k$ we find

$$\frac{\Delta t}{\Delta z} \sim \frac{D}{\nu}. \tag{B.11}$$

This indicate a small time step at the early stages of boundary layer evolution and a much larger step when the boundary layer is well developed. There is absolutely no principal problem employing a variable time step with (B.6), but this is not yet generally implemented.

B.4.2 Test problem

The Crank-Nicholson method, as employed in (B.6) is one of the standard techniques for solution of the heat equation. Still, the implementation must be verified and the performance tested for a relevant boundary value problem. The similarity solution for constant outer velocity is such a problem.
For $U(t) \equiv 1$ and $F \equiv 0$ we have the simple similarity solution

$$w(z) = \frac{2}{\pi} \int_0^{\frac{z}{2\sqrt{\nu t}}} e^{-s^2} ds. \tag{B.12}$$

As $t \to 0$ the solution becomes discontinuous. Naturally, this feature cannot be captured by the finite difference model. Still, this abrupt onset of the boundary layer is relevant for the swash zone in run-up on beaches and it is crucial that the model rapidly produce a reasonably good solution even though the very first phase of the boundary layer evolution is beyond its capacity.
The criterion (B.11) now yields

$$\frac{\Delta t}{\Delta z} \sim \sqrt{\frac{t}{\nu}}.$$

Of course, for fixed grid increments and small t the power expansion leading to (B.10), and thereby to (B.11), becomes inappropriate. Formally, a relative error measure , E, of (B.10) become

$$E = \frac{\Delta z^2}{48\nu t} + \frac{\Delta t^2}{192 t^2},$$

where the factors in the denominators are speculative, but they are hardly less appropriate than 1. For a given resolution the above expression may tell at

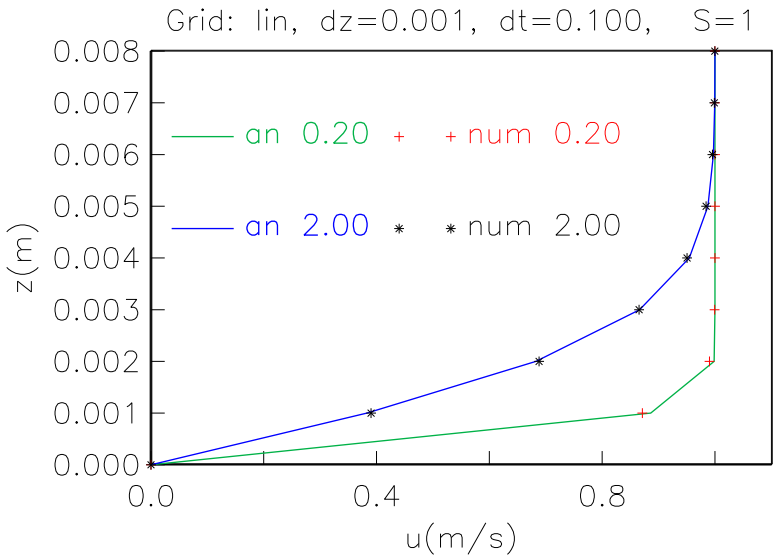

Figure B.2: Simulations of similarity profiles for $t = 0.2\,\mathrm{s}$ and $t = 2\,\mathrm{s}$. Times and lengths are given in seconds and meters, respectively. Analytical and numerical results are marked by "an" and "num" respectively.

which t we may hope to obtain reasonable numerical results. Still, boundary layer development is an accumulative process and the inadequacy of the numerical procedure in relation to the initial discontinuity in the velocity profile may prevail for quite some time after the local error measure E becomes small.
Preferably, an error analysis should be based on the particular solution (B.12) instead of simple harmonics. However, even though local discretization errors may readily be estimated it is a challenging task to link this to errors in the solution itself, particularly in view of the singularity at $t = 0$. Hence, we resort to numerical testing, for now.
If the figures B.2 and B.3 results for a moderately large and a large time are displayed. We immediately observe that the similarity solution is reproduced well.

- For $t = 0.2\,\mathrm{s}$ we observe that convergence appears to more sensitive to Δt than to E.
- For $t = 2.0\,\mathrm{s}$ the given size of Δz for the exponential grid may not be relevant since the smallest Δz is listed in the caption.
- For the finer grids there is a striking similarity between the errors for $t = 0.2\,\mathrm{s}$ and $t = 2\,\mathrm{s}$. This indicate that error is dominated by the errors produced in the abrupt start which then are diffused outward.

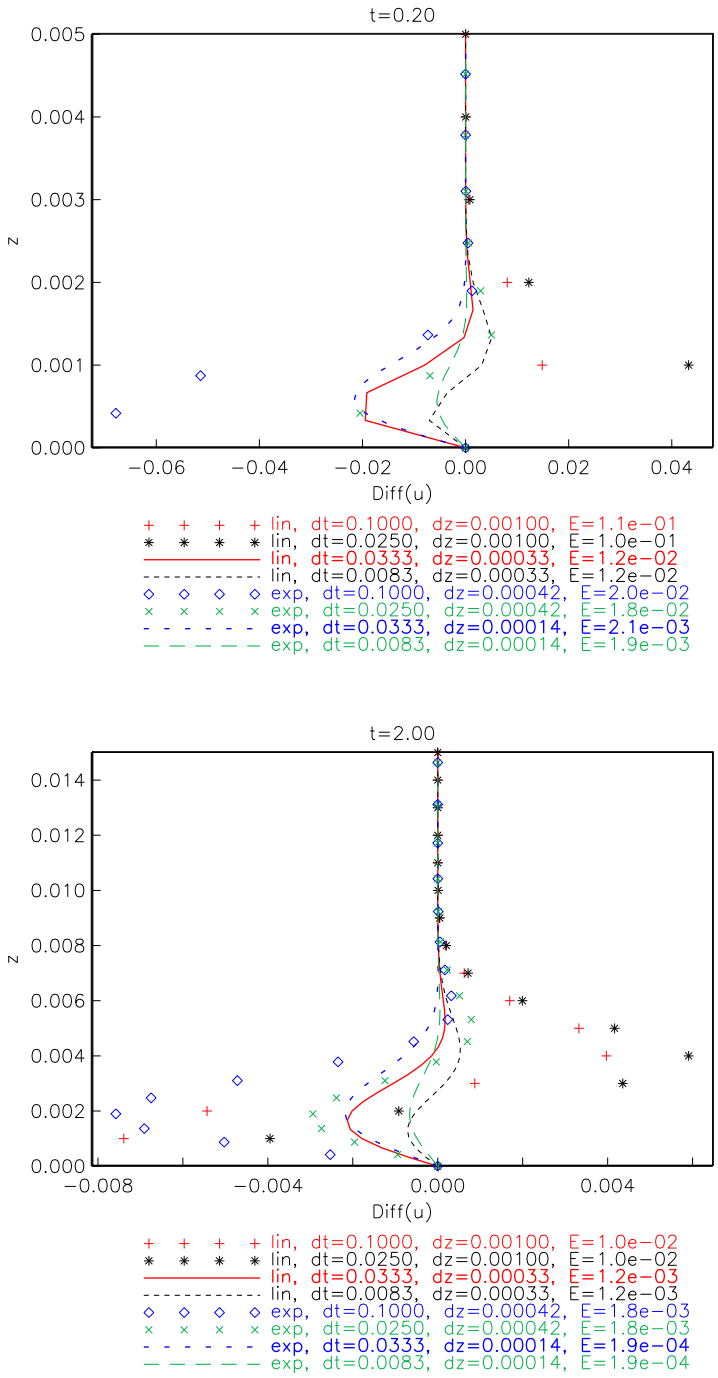

Figure B.3: Errors in simulations of similarity profiles. Times and lengths are given in seconds and meters, respectively. For the exponential grids a strech factor $S = 5$ is employed.

Appendix C

Quality of the gauges

To check the quality of the signal of the gauges, the gauges are set to sample for 2 seconds over a calm surface. The height above the surface is systematically varied so that the gauges record different amplitudes and should confirm the displacement of the gauge. The incoming signal is evaluated, given in the tables below. σ is the standard deviation, $\bar{x}$ is the mean vaule of the signal, conf.int is the confidence interval of the signal and deviation is the deviation from the specific amplitude. The unit is centimeter.

Gauge 1				
amplitude	σ	$\bar{x}$	conf.int (95%)	deviation
5	0.0055	4.9705	[4.9695 4.9715]	0.0295
4	0.0047	3.9784	[3.9775 3.9792]	0.0216
3	0.0047	3.0056	[3.0048 3.0065]	-0.0056
2	0.0059	2.0065	[2.0054 2.0076]	-0.0065
1	0.0047	1.0060	[1.0052 1.0069]	-0.0060
0	0.0050	0.0168	[0.0159 0.0177]	-0.0168
-1	0.0052	-0.9767	[-0.9776 -0.9758]	-0.0233
-2	0.0059	-1.9618	[-1.9628 -0.9607]	-0.0382
-3	0.0078	-2.9703	[-2.9717 -2.9689	-0.0297
-4	0.0060	-3.9696	[-3.9706 -3.9685]	-0.0304
-5	0.0014	-4.9761	[-4.9764 -4.9759]	-0.0239

Gauge 2				
amplitude	σ	$\bar{x}$	conf.int (95%)	deviation
5	0.0018	4.9741	[4.9738 4.9745]	0.0259
4	0.0212	4.0092	[4.0053 4.0130]	-0.0092
3	0.0035	2.9845	[2.9838 2.9851]	0.0155
2	0.0032	1.9776	[1.9770 1.9782]	0.0224
1	0.0031	0.9562	[0.9557 0.9568]	0.0438
0	0.0032	-0.0581	[-0.0587 -0.0576]	0.0581
-1	0.0033	-1.0309	[-1.0315 -1.0303]	0.0309
-2	0.0028	-2.0714	[-2.0719 -2.0709]	0.0714
-3	0.0034	-3.0665	[-3.0671 -3.0659	0.0665
-4	0.0042	-4.0743	[-4.0751 -4.0736]	0.0743
-5	0.0015	-4.9802	[-4.9804 -4.9799]	-0.0198

Gauge 3				
amplitude	σ	$\bar{x}$	conf.int (95%)	deviation
5	0.0031	4.9589	[4.9583 4.9594]	0.0411
4	0.0033	3.9803	[3.9797 3.9809]	0.0197
3	0.0035	2.9845	[2.9838 2.9851]	0.0155
2	0.0030	1.9691	[1.9686 1.9696]	0.0309
1	0.0032	0.9583	[0.9577 0.9589]	0.0417
0	0.0033	-0.0542	[-0.0548 -0.0536]	0.0524
-1	0.0043	-1.0436	[-1.0444 -1.0428]	0.0436
-2	0.0034	-2.0596	[-2.0602 -2.0590]	0.0596
-3	0.0037	-3.0813	[-3.0819 -3.0806]	0.0813
-4	0.0042	-4.0814	[-4.0822 -4.0807]	0.0814
-5	0.0016	-4.9880	[-4.9883 -4.9877]	-0.0120

Gauge 4				
amplitude	σ	$\bar{x}$	conf.int (95%)	deviation
5	0.0115	4.9454	[4.9433 4.9475]	0.0546
4	0.0243	3.9668	[3.9624 3.9712]	0.0332
3	0.0178	2.9520	[2.9488 2.9552]	0.0480
2	0.0090	1.9495	[1.9479 1.9512]	0.0505
1	0.0064	0.9379	[0.9367 0.9390]	0.0621
0	0.0077	-0.0684	[-0.0698 -0.0670]	0.0684
-1	0.0037	-1.0892	[-1.0899 -1.0885]	0.0892
-2	0.0033	-2.1086	[-2.1092 -2.1080]	0.1086
-3	0.0030	-3.1088	[-3.1094 -3.1083	0.1088
-4	0.0100	-4.1145	[-4.1163 -4.1127]	0.1145
-5	0.0008	-4.9920	[-4.9921 -4.9918]	-0.0080

Also, the quality of the signal due to the angular position of the target is evaluated. The gauge is set tho sample for 2 seconds with zero amplitude, the angle is controlled with a digital level and is variated by changing the angle of the gauge. The result is given in the table below, where adj.deviation is the deviation adjusted with the increased distance to the surface due to the angle.

Gauge 1					
angle	σ	$\bar{x}$	konf.int (95%)	deviation	adj.deviation
0	0.0087	-0.0158	[-0.0174 -0.0142]	0.0158	0.0158
1	0.0089	-0.0108	[-0.0124 -0.0092]	0.0108	0.0040
2	0.0045	-0.0378	[-0.0387 -0.0370]	0.0378	0.0105
3	0.0122	-0.0092	[-0.0114 -0.0070]	0.0092	-0.0523
4	0.0048	-0.0487	[-0.0496 -0.0478]	0.0487	-0.0607
5	0.0043	-0.1420	[-0.1428 -0.1412]	0.1420	-0.0291
6	0.0046	-0.2387	[-0.2395 -0.2379]	0.2387	-0.0081
7	0.0049	-0.2145	[-0.2153 -0.2136]	0.2145	-0.1219
8	0.0043	-0.2871	[-0.2879 -0.2864	0.2871	-0.1532
9	0.0043	-0.4418	[-0.4426 -0.4410]	0.4418	-0.1166
10	0.0045	-0.5530	[-0.5538 -0.5522]	0.5530	-0.1381

Appendix D

Matlab code

Tracing of the moving shoreline

```
function shore_trac()


jpegfiles = dir('run4_lower_000*.jpg');
numfiles = length(jpegfiles);
mydata = cell(1,numfiles);
impos = cell(1,numfiles);
filt = cell(1,numfiles);
bwdata = cell(1,numfiles);
edgepos = cell(1,numfiles);
tid = cell(1,numfiles);
edgepixel = cell(1,numfiles);


[x,y]=meshgrid(1:1024,1:1024);
base = [10 2;12 2;14 2;16 2;10 -2; 12 -2;14 -2;16 -2];
input = [583 512;582 439;582 367;582 294;438 512;438 440;438 367;437 295];

tform = cp2tform(base,input,'linear');
[u,v]=tforminv(tform,x,y);

t = 5.5;

for k=1:numfiles

    mydata{k} = imread(jpegfiles(k).name);
    impos{k} = graythresh(mydata{k});
    filt{k} = imopen(mydata{k},strel('disk',20));
    bwdata{k}  = edge(filt{k},'canny',impos{k});
```

```
    tid{k} = t;
    t = t+1/250;
    idx = find(bwdata{k}==1);
    edgepos{k} = median(u(idx));
    edgepixel{k} = median(y(idx));

end


pos = cell2mat(edgepos);
pospix = cell2mat(edgepixel);
tid2 = cell2mat(tid);

fid = fopen('utfil_case10_run3_coord1','w');
   for i=1:numfiles
      fprintf(fid,'%f %f\n',tid2(i),pos(i));
   end
 fclose(fid);

 fid = fopen('utfil_case10_run3_coord1_pix','w');
    for i = 1:numfiles
    fprintf(fid, '%f\n',pospix(i));
    end
 fclose(fid);
```

List of Figures

Bibliography

[1] G. K. Pedersen and B. Gjevik. Run-up of solitary waves. *Journal of fluid mechanics*, 135:283–299, 1983.

[2] C. E. Synolakis. The runup of solitary waves. *Journal of Fluid Mechanics*, 185:523–545, 1987.

[3] Y. Li and Raichlen F. Solitary wave runup on plane slopes. *Journal of Waterway, Port, Coastal, and Ocean Engineering*, 127:33–44, 2001.

[4] Y. Li and F. Raichlen. Non-breaking and breaking solitary wave run-up. *Journal of Fluid Mechanics*, 456:295–318, 2002.

[5] A. Jensen, G. Pedersen, and D. J. Wood. An experimental study of wave run-up at a steep beach. *Journal of fluid mechanics*, 486:161–188, 2003.

[6] G. Sælevik. *Particle Image Velocimetry applied to complex flows in a wave tank*. PhD thesis, University of Oslo, 2009.

[7] P. L.-F Liu, Y. S. Park, and Cowen E. A. Boundary layer flow and bed shear stress under a solitary wave. *Journal of Fluid Mechanics*, 574:449–463, 2007.

[8] B. Mutlu Sumer, P. M. Jensen, L. B. Sørensen, J. Fredsøe, P. L.-F Liu, and S. Carstensen. Coherent structures in wave boundary layers. part 2. solitary motion. *Journal of fluid mechanics*, 646:207–235, 2009.

[9] K. P. Kundu and Cohen M. P. *Fluid Mechanics*. Academic press, fourth edition, 2008.

[10] J. N. Newman. *Marine Hydrodynamics*. Massachusetts Institute of Technology, first edition, 1977.

[11] B. Gjevik. *Forelesninger i bølgeteori*. Universitetet i Oslo, 2005.

[12] F. M. White. *Viscous fluid flow*. Mc Graw Hill, third edition, 2006.

[13] G. Pedersen. Modeling runup with depth integrated equation models. In P. L. F. Liu and C. Synolakis, editors, *Advanced numerical models for simulating tsunami waves and runup*, pages 3–42.

[14] G. Pedersen. Modeling runup with depth integrated equation models. In P. L. F. Liu and C. Synolakis, editors, *Advanced numerical models for simulating tsunami waves and runup*, pages 3–42.

[15] J. K. Sveen and E. A. Cowen. Quantitative imaging techniques and their applications in wavy flows. In J. Grue, P. L. F. Liu, and G. Pedersen, editors, *PIV and water waves*, pages 1–49.

[16] M. Raffel, C. Willert, S. Wereley, and J. Kompenhans. *Particle Image Velocimetry: A practical guide*. Springer, second edition, 2007.

[17] S. Dalziel. Digiflow. http:// www.dalzielresearch.com/digiflow, 2008.

[18] B. M. Sumer, P. M. Jensen, L. B. Sørensen, J. Fredsøe, P. L.-F Liu, and S. Carstensen. Coherent structures in wave boundary layers. part 2. solitary motion. *Journal of Fluid Mechanics*, 646:207–231, 2010.

[19] M.J. Cooker, D.H. Peregrine, C. Vidal, and J.W Dold. The interaction between a solitary wave and a submerged semicircular cylinder. *Journal of Fluid Mechanics*, 215:1–22, 1990.

[20] J. W. Dold. An efficient surface-integral algorithm applied to unsteady gravity waves. *J. Comp. Phys.*, 103:90–115, 1992.

[21] S. Grilli and I. A. Svendsen. Computation of nonlinear wave kinematics during propagation and run-up on a slope. In *Water wave kinematics*, pages 387–412.

[22] S.T. Grilli, R. Subramanya, I.A. Svendsen, and J. Veeramony. Shoaling of solitary waves on plane beaches. *J. Wtrwy., Port, Coast., and Oc. Engrg.*, 1994.

[23] S.T. Grilli, I.A. Svendsen, and R. Subramanya. criterion and characteristics for solitary waves on slopes. *J. Wtrwy., Port, Coast., and Oc. Engrg.*, 1997.